JAMES | Journal of Advances in Modeling Earth Systems

RESEARCH ARTICLE
10.1029/2019MS001736

What Drives the Life Cycle of Tropical Anvil Clouds?

Blaž Gasparini[1], Peter N. Blossey[1], Dennis L. Hartmann[1], Guangxing Lin[2], and Jiwen Fan[2]

[1]University of Washington, Seattle, WA, USA, [2]Pacific Northwest National Laboratory, Richland, WA, USA

Key Points:
- Both radiative and latent heating within anvil clouds strongly influence the cloud radiative effect at the top of the atmosphere
- Latent and radiative heating drive turbulence and organized circulations within the anvil cloud structure
- Radiative heating dominates near the top of the cloud, while latent heating dominates near the base of the cloud

Supporting Information:
- Supporting Information S1
- Movie S1
- Movie S2

Correspondence to:
B. Gasparini,
blazg@uw.edu

Citation:
Gasparini B., Blossey, P. N., Hartmann, D. L., Lin, G., & Fan, J. (2019). What drives the life cycle of tropical anvil clouds? *Journal of Advances in Modeling Earth Systems*, *11*, 2586–2605. https://doi.org/10.1029/2019MS001736

Received 8 MAY 2019
Accepted 16 JUL 2019
Accepted article online 25 JUL 2019
Published online 13 AUG 2019

Abstract The net radiative effects of tropical clouds are determined by the evolution of thick, freshly detrained anvil clouds into thin anvil clouds. Thick anvil clouds reduce Earth's energy balance and cool the climate, while thin anvil clouds warm the climate. To determine role of these clouds in climate change we need to understand how interactions of their microphysical and macrophysical properties control their radiative properties. We explore anvil cloud evolution using a cloud-resolving model in three-simulation setups of increasing complexity to disentangle the impacts of the various components of diabatic heating and their interaction with cloud-scale motions. The first phase of evolution and rapid cloud spreading is dominated by latent heating within convective updrafts. After the convective detrainment stops, most of the spreading and thinning of the anvil cloud is driven by cloud radiative processes and latent heating. The combination of radiative cooling at cloud top, latent cooling due to sublimation at cloud base, latent heating due to deposition and radiative heating in between leads to a sandwich-like, cooling-heating-cooling structure. The heating sandwich promotes the development of two within-anvil convective layers and a double cell circulation, dominated by strong outflow at 12-km altitude with inflow above and below. Our study reveals how small-scale processes including convective, microphysical processes, latent and radiative heating interact within the anvil cloud system. The absence or a different representation of only one component results in a significantly different cloud evolution with large impacts on cloud radiative effects.

Plain Language Summary Clouds have a large influence on climate. Thick clouds reflect part of the solar (or shortwave) radiation back to space and therefore cool the climate. On the other hand, wispy and thin high clouds do not reflect much of solar radiation. They form high in the atmosphere at cold temperatures and therefore keep part of the terrestrial (or longwave) radiation within the atmosphere. They warm the climate, similarly to greenhouse gasses. The evolution of thunderstorm clouds is of particular interest as it involves a transition from the thick clouds that cool the climate to the thin high clouds that warm the climate. We study small-scale processes that drive this transition and their delicate balance and interactions. Tiny differences in how ice crystals form, grow, shrink, or interact with solar or terrestrial radiation can lead to large differences in the climatic role of thunderstorm clouds. Such processes are currently not represented in models we use for climate projections. Our findings may ultimately lead to improvements in the representation of thunderstorm cloud life cycles in climate models and therefore increase the trust in projections of future climate.

1. Introduction

In the tropical regions of prevalent ascent, clouds strongly modulate both the shortwave (SW) and longwave (LW) radiative fluxes, leading to large SW and LW cloud radiative effects (CRE; Ramanathan et al., 1989). High ice clouds cover a large fraction of the tropics (Martins et al., 2011; Sassen et al., 2009). While the thickest precipitating high clouds have both large SW and large LW CRE, they are not the most dominant cloud type radiatively due to their short lifetime and limited spatial coverage. They fundamentally control the tropical CRE, however, through detrainment of large quantities of ice crystals (ICs). These crystals form anvil clouds, which spread over surface areas much larger than the deep convective cores from which they originate (Protopapadaki et al., 2017). Their combination of a moderate CRE and frequent occurrence makes detrained ice clouds the radiatively most important high cloud type in the tropics (Berry & Mace, 2014; Hartmann & Berry, 2017). Moreover, previous observational and modeling studies have shown that at least 50% of all ubiquitous tropical thin cirrus directly originates from deep convective sources (Gasparini et al., 2018; Gehlot & Quaas, 2012; Luo & Rossow, 2004; Massie et al., 2002; Riihimaki et al., 2012).

The life cycle of anvil clouds is controlled by a number of processes including radiative heating due to in-atmospheric cloud radiative effects (ACRE), latent heating, microphysical processes like IC nucleation and growth, IC sedimentation, mixing of environmental air across cloud interfaces, turbulence, and cloud-scale circulations. However, it is still not fully understood what the main drivers of anvil cloud extent are, their microphysical and radiative properties, nor what controls the tropical CRE. Moreover, it is not clear whether the delicate balance between small-scale processes can change in a warmer climate, and what could be the climatic impacts of such a change.

Ackerman et al. (1988) were the first to quantify the radiative heating rates within tropical anvils based on in situ aircraft data. The measured anvils were dominated by the LW warming effect, concentrated near cloud base, and LW cooling at the cloud top, that coincides with a minor SW warming effect. They hypothesized that the large heating gradients can lead to convective instability within an anvil. Their ideas were formalized in theoretical work by Lilly (1988) who proposed a two-stage model of the cirrus convective outflow. The initial outflow of air of nearly uniform buoyancy from the convective core flattens and stretches shortly after being injected into a stably stratified environmental air. The following stage is driven by differential radiative heating, forming a self-maintaining radiative convective mixed layer within an anvil. The existence of within-anvil convective motions was confirmed by numerous observational and modeling studies (Dobbie & Jonas, 2001; Durran et al., 2009; Dinh et al., 2010; Ferlay et al., 2014; Jensen et al., 2009; Harrop & Hartmann, 2016). However, both Ackerman et al. (1988) and Lilly (1988) neglected the latent heating, which leads to strong heating by deposition and freezing throughout most of the anvil, and cooling at and below-cloud base due to sublimation, melting, and evaporation of precipitation (Houze, 1982; Liu et al., 2015; Lohmann & Roeckner, 1995; Schumacher et al., 2004; Starr & Cox, 1985). The anvil cloud extent and its lifetime were found to be sensitive to the IC size and number concentration. Fan et al. (2010, 2013) showed how different specifications of cloud condensation nuclei and ice nucleating particles led to differing anvil cloud properties. Moreover, tropical anvil cloud properties were found to be very sensitive to the level of turbulent mixing simulated by the model (Ohno et al., 2019). Hartmann et al. (2018) found that ACRE promote the formation and maintenance of thin anvils with the help of two-dimensional cloud-resolving model simulations. ACREs increase the longevity of thin anvils by microphysical cycling of water vapor and ICs within the in-cloud convective mixed layer. This ACRE-driven mechanism was crucial to achieve a balanced net CRE. Our study expands on that work by using three-dimensional simulations allowing the cloud to evolve by spreading into its surrounding, cloud-free environment.

Previous studies focused only on one phase or one aspect of the anvil life cycle, while we want to explore the main small-scale drivers over the whole life cycle, from the thick deep convective cloud to the thin cirrus. Therefore, we set up simulations of three increasing levels of complexity:

- a thick ice cloud in the middle of a cloud-free domain, initially in buoyant equilibrium with the environment;
- an isolated tropical deep convective system, in which we follow the cloud from the convective initiation from a warm, moist bubble until its decay;
- a longer, "climatological" simulation of radiative convective equilibrium (RCE), in which we statistically cluster the information over a large ensemble of convective events that maintain RCE.

Having simulations of differing complexity increases the robustness of the results and underlines the importance of small-scale processes in driving of the spreading and thinning of anvil clouds.

2. Modeling Setup

We use System for Atmospheric Modeling (SAM) cloud-resolving model (Khairoutdinov & Randall, 2003) version 6.10. The simulations use a 256- × 256-km domain with a horizontal resolution of 1 km and vertical resolution of 250 m in the upper troposphere, except for the RCE simulations (described in section 2.3). The model top is at 27 km. The longer duration RCE simulations use a smaller, 128- × 128-km horizontal domain with the same vertical grid. SAM is a nonhydrostatic anelastic model with periodic lateral boundary conditions coupled with the RRTMG radiative transfer model (Iacono et al., 2008; Mlawer et al., 1997). Subgrid-scale motions are represented with a 1.5-order closure scheme that incorporates a simple Smagorinsky-type scheme. We coupled the model with the Predicted Particle Properties (P3) bulk microphysical scheme (Morrison & Milbrandt, 2015), version 2.8.2.4. P3 avoids the artificial separation of ice particles into its floating and precipitating parts; instead, it uses four prognostic variables that track the

Table 1
Simulation Terminology and Their Respective Properties

Simulation	Description
1. Isolated cloud	
CTRL_cld	256 × 256 horizontal grid boxes with 1-km resolution; 128 vertical levels with 250-m resolution in the upper troposphere
NO ACRE	As *CTRL_cld* but no interactive ACRE
NO SUBI	As *CTRL_cld* but with no sublimation of ICs
NO DEPO	As *CTRL_cld* but no deposition of vapor on ICs
NO NUCI	As *CTRL_cld* but with no new nucleation of ICs
NO SEDI	As *CTRL_cld* but with no sedimentation ICs
2. Isolated convection	
CTRL_con	256 × 256 horizontal grid boxes with 1-km resolution; 128 vertical levels with 250-m resolution in the upper troposphere
VRES_con	As *CTRL_con* but with 256 vertical levels with 50 m upper tropospheric grid spacing
HRES_con	As *VRES_con* but with 640 × 640 horizontal boxes of 250-m grid spacing
NFRZ_con	As *CTRL_con* but with different freezing for temperatures colder than −38 °C
IClim05_con	As *CTRL_con* but with the upper IC number limit of 0.5×10^3 kg^{-1}
IClim100_con	As *CTRL_con* but with the upper IC number limit of 100×10^3 kg^{-1}
3. RCE	
CTRL_rce	128 × 128 horizontal grid boxes with 1-km resolution; 128 vertical levels with 250-m resolution in the upper troposphere
CTRL0.25-7_rce	As *CTRL_rce* but with a horizontal grid spacing of 0.25, 0.5, 2, 3, 5, and 7 km
IClim0.5_rce	As *CTRL_rce* but with the upper IC number limit of 0.5×10^3 kg^{-1}
IClim100_rce	As *CTRL_rce* but with the upper IC number limit of 100×10^3 kg^{-1}
NFRZ_rce	As *CTRL_rce* but with different freezing for temperatures colder than −38 °C

mixing ratios of total ice mass, total ice number, rime mass, and rime volume. Therefore, instead of specifying particle properties for several ice types (e.g., floating ice, snow, and graupel), the scheme uses its 4 degrees of freedom to predict them. The scheme avoids artificial boundaries between particle types and avoids unphysical thresholds like the autoconversion radius of transition of ice to snow. P3 is therefore well suited for studies of transitions of deep, precipitating anvils, to thin, nonprecipitating cirrus; a situation, in which we expect numerous transitions between several categories of atmospheric ice particles. In order to allow the formation of clouds with number concentrations of ICs comparable to those observed in freshly detrained anvil clouds (Heymsfield, Krämer, Luebke, et al., 2017; Jensen et al., 2018), we increased the upper limit of IC number concentration from 0.5×10^6 to 10^7 kg^{-1} (about 2–5 $\times 10^3$ L^{-1} at the anvil cloud altitudes). Simulations of the dynamics of the MJO field campaign (Yoneyama et al., 2013) that used this increased upper limit on the IC number concentration showed good agreement with the observed radiative fluxes (Gasparini et al., 2018). The generalized effective IC size predicted by P3 is used in the computation of radiative fluxes.

For simplicity, diurnally averaged insolation is used with a solar zenith angle of 42.89° and insolation (423.5 W/m^2) representative of the annual mean values in the tropics. The simulations are initialized without the presence of any mean winds and are not nudged. Sea surface temperature is fixed at 30 °C. The simulations are described in Table 1.

We show two idealized modeling setups which represent the evolution of an idealized anvil cloud. The simplest, isolated cloud setup neglects the initial step of the cloud formation by focusing purely on the evolution and cloud thinning. The isolated convective setup, on the other hand, represents the whole convective (and anvil) life cycle, including the detrainment step. Finally, the RCE setup is used to study climatological properties over a large ensemble of anvil cloud life cycles.

2.1. Isolated Cloud

We initialize the simulation with an optically thick high cloud (cloud optical depth, COD, of 120) of uniform ice water content (IWC; 0.3 g/m^3), which fits within the range of both in situ and remote sensing

observations of tropical anvil clouds (Garrett et al., 2005; Heymsfield, Krämer, Wood, et al., 2017; Heymsfield, Krämer, Luebke, et al., 2017). This simulation setup represents a freshly detrained anvil cloud, after most of the convective activity has ceased. The initial mean IC size is prescribed to follow observations by Van Diedenhoven et al. (2016), with an effective radius of 20 μm close to the cloud top, which increases linearly to reach 40 μm at the cloud base. The IC number concentration spans the range between 900 and 3,600 L^{-1}, with the lowest concentrations at cloud base, and concentration higher than 3,000 L^{-1} above 10.5 km, which lies well within the range of in situ observations (Jackson et al., 2015; Krämer et al., 2016; Heymsfield, Krämer, Luebke, et al., 2017). The cloud is initialized with random potential temperature perturbations of the order of 0.01 °C, to help start the development of within-anvil motions. The cloud is 5-km thick with a top at 13- and base at 8-km altitude, which corresponds to the peak of the cloud cover in tropical convective regions (Hartmann & Berry, 2017; Protat et al., 2010). The cloud is initially in buoyant equilibrium with the surrounding environmental air. It is initialized with a radius of 30 km centered in the middle of the model domain, a 256-km square.

2.2. Isolated Convection

We first decrease the specific humidity in the lowermost 3 km of the domain by 20% with respect to the typical tropical moisture profile to suppress convective plumes. The temperature profile is near the moist adiabat at all altitudes. Second, we initialize the simulation with a sinusoidal moisture perturbation with a peak of 5 g/kg, which decays both in the vertical and horizontal dimensions. The perturbation extends up to 3 km in vertical and 30 km in horizontal from its mid point. Such model initialization ensures that convection starts first in the middle of the model domain and preserves a large degree of its azimuthal uniformity throughout the convective life cycle, due to the lack of any environmental winds.

We can decompose the total heating rate into the radiative (cloudy and clear sky) and latent heating component with an additional residual term related mainly to unresolved turbulent motions as

$$\frac{\mathrm{d}T}{\mathrm{d}t} = Q_{\mathrm{rad,cld}} + Q_{\mathrm{rad,cs}} + Q_{\mathrm{latheat}} + Q_{\mathrm{residual}} \tag{1}$$

where T is temperature, t is time, and Q are the heating rates. We diagnose each of them directly from the model. We use azimuthal averaging, with the center of the domain (which is also the center of the cloud) being the center point of our cylindrical coordinate system.

The absence of geostrophic motions in the tropics results in weak horizontal temperature gradients (Charney, 1963). Therefore, we use the weak temperature gradient approximation (e.g., Sobel & Bretherton, 2000) to derive the vertical velocities associated with each of the heating terms using

$$w\frac{\partial s}{\partial z} = Qc_p \tag{2}$$

where w is the azimuthally averaged vertical velocity and s is the dry static energy ($s = c_p T + gz$). We compute the residual vertical velocity as follows:

$$w_{\mathrm{residual}} = w_{\mathrm{total}} - w_{\mathrm{rad,cld}} - w_{\mathrm{rad,cs}} - w_{\mathrm{latheat}} \tag{3}$$

Finally, we derive the total stream function from various heating sources (radiative, latent, and residual) by integrating the following equation in cylindrical coordinates over the radial dimension:

$$\frac{\partial \psi_i}{\partial r} = rw_i \tag{4}$$

$$\psi_i = \int_0^r rw_i \mathrm{d}r \tag{5}$$

where r is the distance from the center of the domain and w_i represent the vertical velocities defined in equation (3).

2.3. RCE

The simulation is started with typical tropical temperature and moisture conditions, which quickly initiates convection. The simulation is run for 80 days, with a 2-hourly instantaneous output time step for the 2-D and 3-D fields. For the purpose of the present analysis, we only consider 48 output time steps from day 70–74 of the simulation, after the climate reached its equilibrium state. The model output is binned by increasing ice water path (IWP) values into 50 equispaced bins, each spanning 2% of all data points.

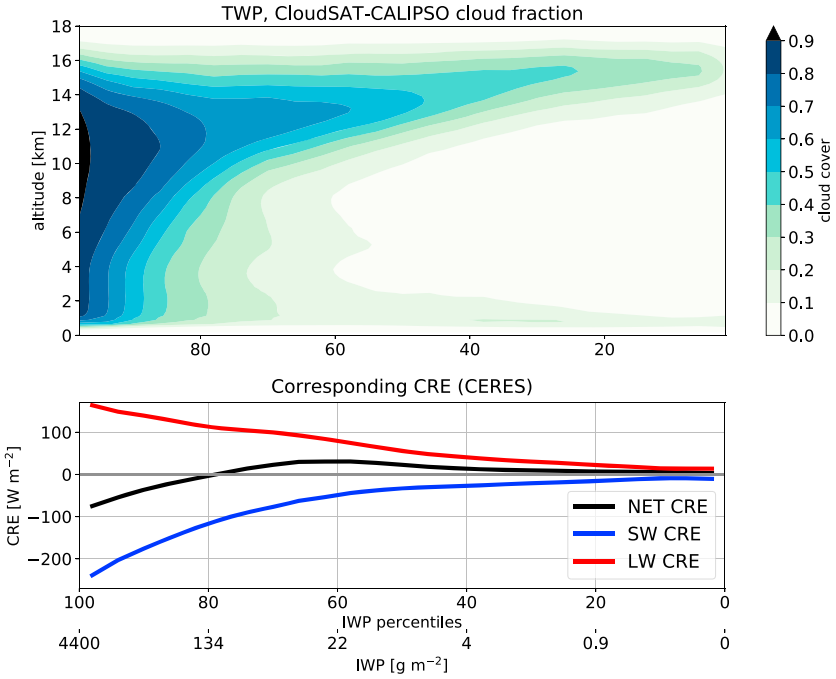

Figure 1. CCCM-derived cloud fraction binned into 25 IWP percentiles for the TWP. Below are plotted the corresponding CRE. CCCM = CALIPSO, CloudSat, CERES, and MODIS Merged Product Release B1; IWP = ice water path: CRE = cloud radiative effects.

3. Observational Data

We use the CALIPSO-CloudSat-CERES-MODIS (CCCM) data set (Kato et al., 2011) for the years 2007–2010. The CCCM data set combines CALIPSO lidar (Winker et al., 2010) and CloudSat radar (Stephens et al., 2008) cloud fraction collocated with MODIS IWP data and CERES radiative fluxes (Wielicki et al., 1996). We derive SW radiative fluxes from CERES, which are available only for daytime. To avoid problems at large solar zenith angles, we limit the data to points with zenith angle smaller than 70°, which restricts us to the afternoon overpass (1.30 p.m.) of the A-Train satellite constellation. We derive the albedo based on the incoming and outgoing SW fluxes at the top of the atmosphere (TOA). The diurnally averaged reflected SW is computed by multiplying the albedo by the daily and annual averaged incoming radiation for the region of 423.5 W/m^2. We use data for the TWP (12°S to 12°N and 150 to 170°E), a region dominated by deep convection year round. The albedo at the TOA and SW CRE are computed as

$$\text{albedo} = \frac{SW_{\text{out}}}{SW_{\text{incoming}}} \tag{6}$$

$$SW_{\text{CRE}} = -(\text{albedo} - \text{albedo}_{\text{clear-sky}}) * 423.5\,\text{W/m}^2 \tag{7}$$

The LW CRE is computed as

$$LW_{\text{CRE}} = OLR_{\text{clear}} - OLR \tag{8}$$

where OLR is outgoing LW radiation at the TOA.

We bin the radiative fluxes and cloud fraction into 25 bins ordered by the percentiles of MODIS-derived IWP, each of them covering 4% of all considered points.

4. Results

Figure 1 shows the observed cloud fraction and its corresponding radiative effects binned by the respective IWP percentile values for the TWP. The high percentiles contain a fully cloud-covered troposphere and therefore represent deep convective towers, with both strong SW and LW CRE, where the SW component

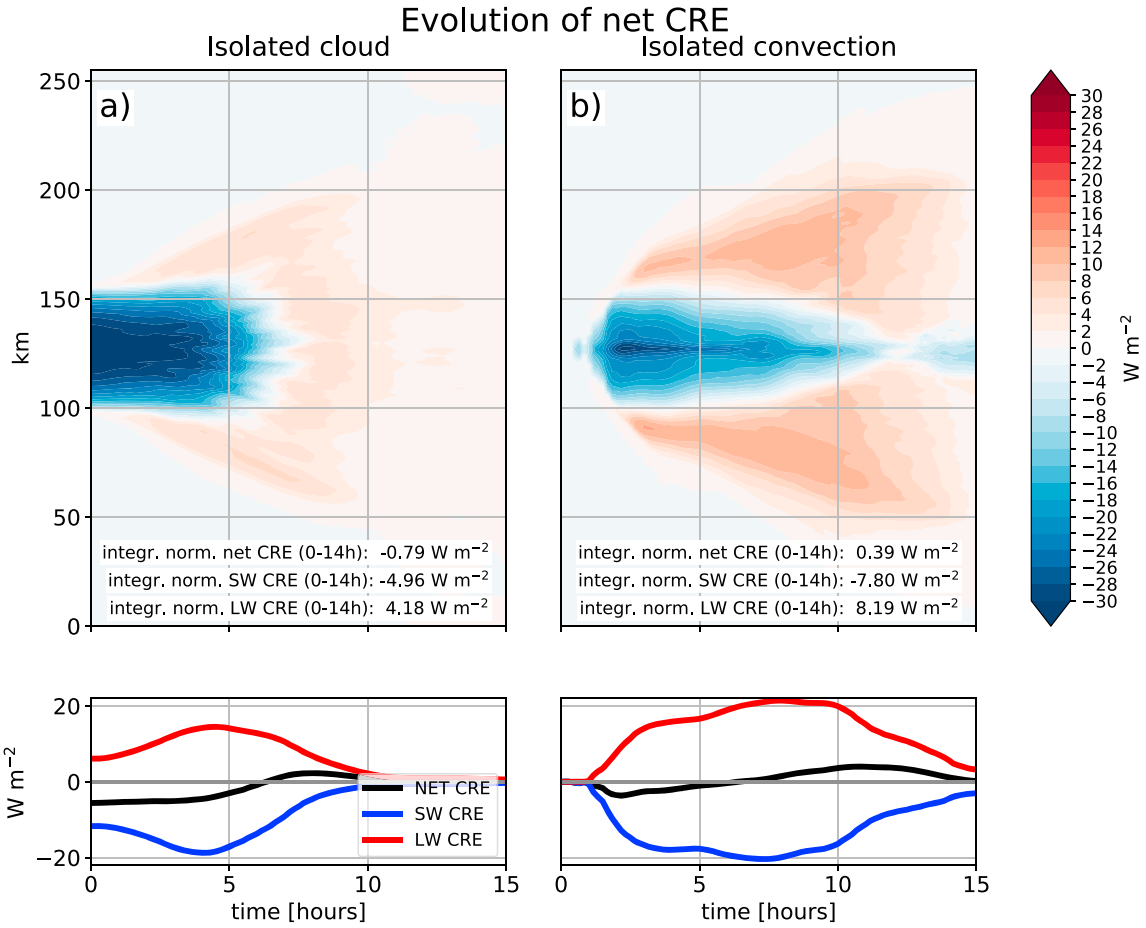

Figure 2. CRE evolution for simulations of an isolated cloud (a) and isolated convection (b). The contour plots are computed by averaging over one of the horizontal dimensions. The lower plot represents the domain-averaged CRE. The numbers represent CRE integrated over the whole life cycle. CRE = cloud radiative effects; SW = shortwave; LW = longwave.

is the dominant one. The intermediately thick anvil clouds that spread from the convective core at 10- to 14-km altitude are responsible for a shift of net CRE from negative to positive close to the 75th IWP percentile. Such clouds contain IWP of 5 to 150 g/m^2 and have COD between 1 and 6, and net CRE of about +5 to −25 W/m^2. The upper tropospheric cloud peak spreads toward higher altitudes when transiting to lower IWP values due to either the in situ formation of new ice clouds or by lofting of anvil remains, as suggested by Hartmann and Berry (2017) and modeled by Hartmann et al. (2018). Remarkably, the net CRE shifts from values around −100 W/m^2 for the highest percentiles, toward +15 to +30 W/m^2 for the 40th to 70th percentiles. The crossover point in net CRE occurs near IWP of 100 g/m^2 and COD of four, roughly at the point where the cloud stops precipitating. The cloud columns maintain on average a net positive CRE even at lower percentiles, in which the tropical tropopause layer cirrus competes with infrequent, yet radiatively important boundary layer clouds. The average net CRE considering all selected clouds is +0.6 W/m^2, very close to being radiatively neutral. The radiative balance in the TWP is therefore controlled by a near-perfect cancelation of the large SW and LW components when integrated over all cloud types. Given the large SW and LW CRE, a small shift in the cloud distribution or its properties could result in large impacts on the radiative balance. This motivates us to study the details of the convective life cycle, with focus on the transition between a freshly detrained, thick anvils and aged, thin anvil cloud remains.

4.1. CRE Evolution

Figure 2 represents the time evolution of net CRE for the simulations of the isolated high cloud (a) and isolated convection (b). The former starts as a thick cloud dominated by its SW CRE. The cloud quickly starts spreading and thinning, increasing the thin cirrus fraction and its contribution to the overall radiative budget. The spreading is evident as both the domain-averaged SW and LW CRE increase in the first 3 hr

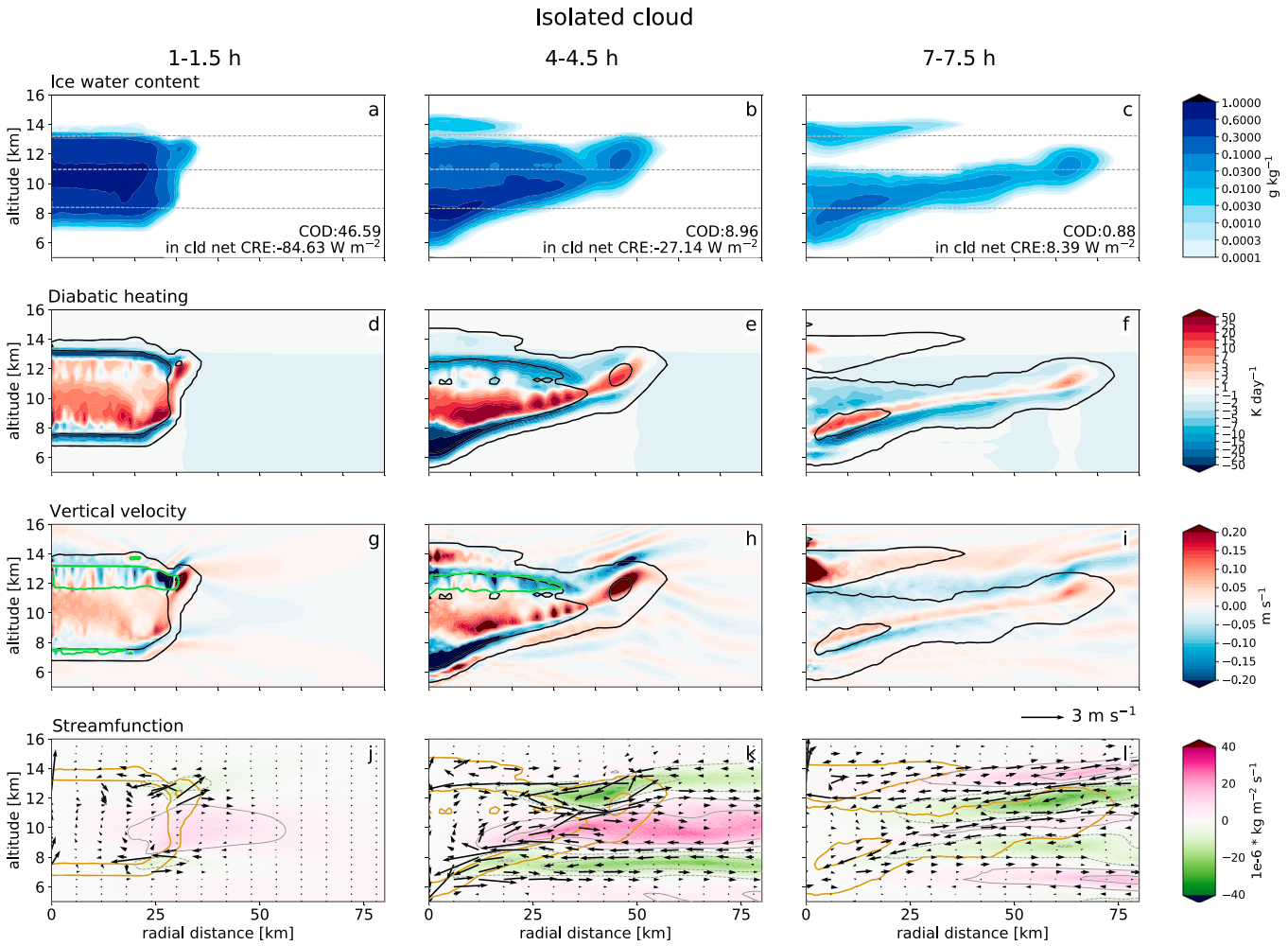

Figure 3. Evolution of the isolated high cloud: IWC (a–c), diabatic heating (d–f), vertical velocity (g–i), and stream function and wind fields (j–l). The plotted timesteps are representative of the intial, mature, and late stage of cloud evolution. The panels (a)–(c) include temperature isolines and in-cloud COD and CRE values. The green contours in panels (g)–(i) are highlight areas of high spatial variability of vertical velocity. The plotted quantities are azimuthally averaged with respect to the center of the domain. The dashed lines in (a)–(c) are isotherms of −20, −40, and −60 °C. Black or brown contour lines represent IWC contours of 0.1 and 0.0001 g/kg. The vertical velocity vectors are multiplied by a factor of 4 to give a better visual representation of circulations. IWC = ice water content; COD = cloud optical depth; CRE = cloud radiative effects.

of the simulation, after which the SW effect decreases at a stronger pace than the LW CRE. This leads to a switch from a net negative to a net positive CRE. The cloud gradually thins until it becomes radiatively unimportant after 10 hr of simulation. The net CRE averaged over the whole life cycle is slightly negative and about an order of magnitude smaller than the individual SW and LW CRE.

In Figure 2b, isolated convection starts to develop quickly after the beginning of the simulation, leading to a small, 10- to 15-km broad convective core. The convection leads to a quickly spreading cloud in the upper troposphere, whose diameter exceeds 100 km after the first 4 hr of the simulation. The cloud is still influenced by the convective detrainment in the first few hours, which generates a thick anvil cloud, dominated by SW CRE. The combination of a decreasing convective detrainment, stratiform precipitation, and spreading of the cloud leads to cloud thinning. The thin part of the cloud significantly modifies the outgoing LW radiative fluxes, despite being almost transparent to the incoming SW radiation. The domain average CRE therefore transits from a net CRE negative to a net CRE positive ~7 hr after the start of the simulation, reaching a peak between hour 11–12. While a thin anvil lingers in the atmosphere, new convective activity starts approximately at hour 13 of the simulation, marking the end of the studied convective life cycle. The domain-averaged integrated value of SW and LW CRE almost perfectly balance each other, yielding only a small, slightly positive net CRE, similarly to the near-cancelation of CRE observed in many tropical areas.

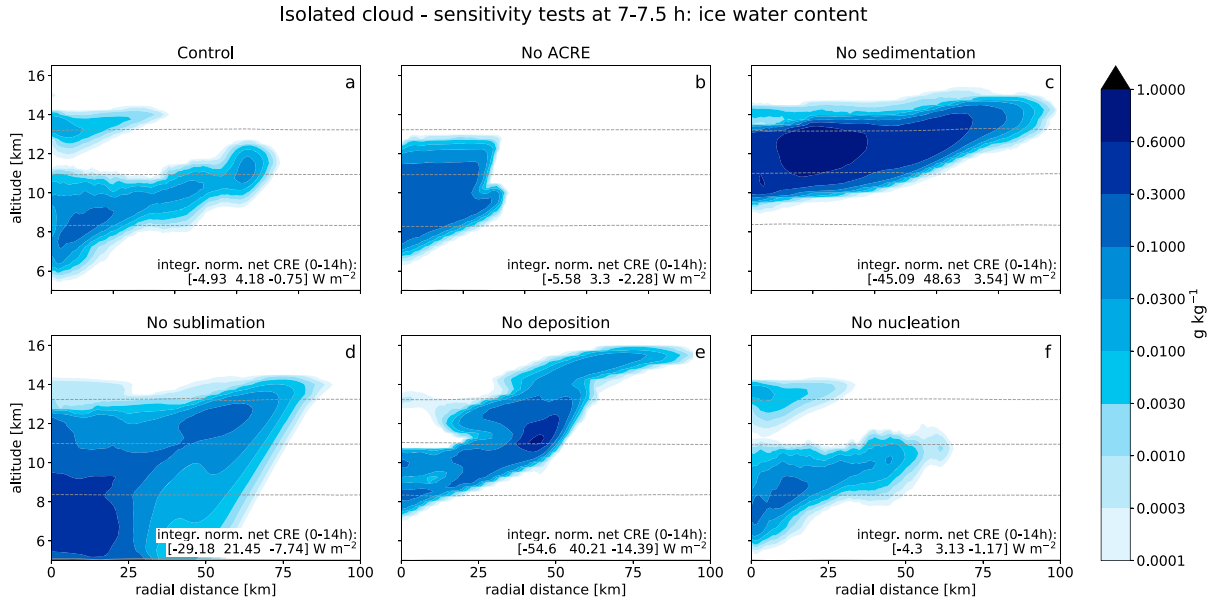

Figure 4. Sensitivity simulations for the isolated clouds (a–f). The numbers at the bottom of the panels represent the integrated values of SW, LW, and net CRE over the first 14 hrs of the respective simulations.

4.2. Isolated High Cloud

We now examine in detail the evolution of the thick cylindrical ice cloud initialized in the middle of the domain.

4.2.1. Initial Phase

The interactions of ICs and radiation instantaneously form a strong cooling of about −70 K/day at the cloud top (Figures 3a and 3d). This LW cooling is partially compensated by the SW heating, which is able to penetrate further toward the interior of the cloud (Figure S1 in the supporting information). The heated air below cloud top becomes positively buoyant and tries to rise above the sinking cool air at the cloud top. This helps establish in-cloud convective motions near cloud top within the first 15–30 min after the start of the simulation (Figure S2). The convective mixed layer is further intensified by the latent heating due to deposition and freezing in updrafts, and latent cooling by sublimation in downdrafts (Figure S2). However, the cloud top mixed layer forms even in experiments in which we turned off deposition (*NO DEPO*) and sublimation (*NO SUBI*, also refer to Table 1), but does not form in the *NO ACRE* simulation. The mixed layer grows in vertical from about 750 m to about 2 km in the first 2 hr, after which it starts decaying. At that point circulations formed by diabatic heating take control of the cloud evolution (Figures 3g, 3h, 3j, 3k, and S2).

Similarly, the strong radiative heating at the cloud base combined with latent cooling by sublimation initiate a short-lived mixed layer just above cloud base 30 min after the beginning of the simulation (Figures 3g and S3). A weak turbulent layer forms also near the peak of latent cooling below the cloud base, which, however, cannot significantly influence the development of the overlying cloud. The *NO SUBI* experiment does not form mixed layers at cloud base, confirming the importance of sublimation for cloud base evolution. However, the absence of sublimation helps form a strong melting layer just below the 0 °C isotherm, initiating small convective motions and a weak circulation pattern (Figures S4 and 4c). The mixed layers at cloud base cannot fully develop due to the IC sedimentation and precipitation that inhibit the overturning motions. Both cloud top and cloud base mixed layers in the NO SEDI experiment continue to grow even beyond the first 2 hr of the simulation, eventually forming a single, self-sustained convective layer between 10- and 14-km altitude (Figure S5).

The spreading of the cloud leads to a bowl-shaped pattern (Figures 3b and 3c), consistent with the work of Schmidt and Garrett (2013). The cloud layer spreads along the isentropes, which are distorted by strong sources of diabatic heating and cooling (Figures 3d–3f). The bowl-shaped spreading still appears in *NO SEDI* (Figure 4g) and is therefore not caused by sedimentation of ICs.

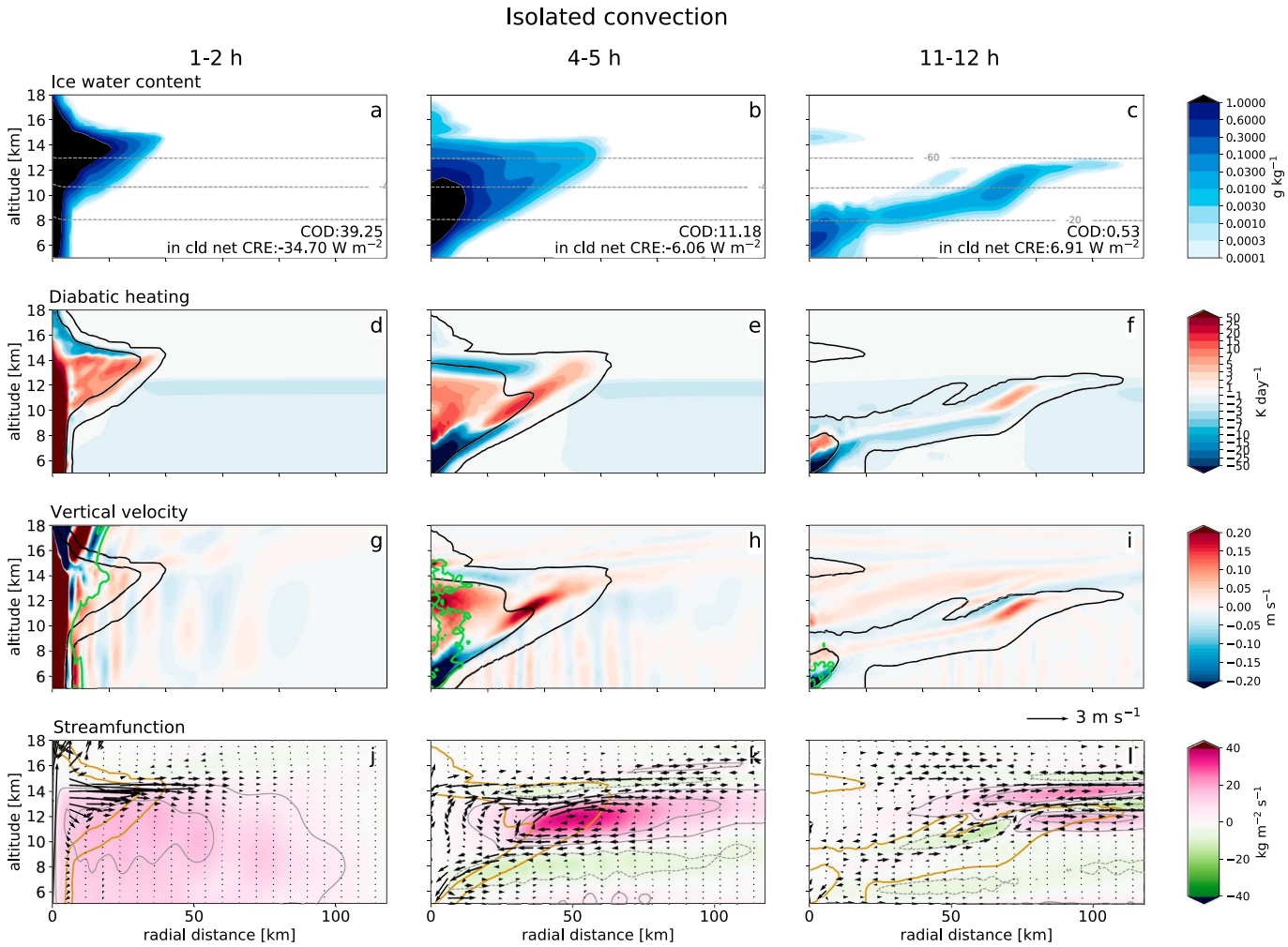

Figure 5. As in Figure 3, but for the isolated convection.

4.2.2. Mature Phase of Development

The mature phase starts with the decay of initial mixed layers and when the diabatically driven circulations become fully developed (Figures 3h and 3k). The initial radiatively driven heating structure now decreases in magnitude with the decreasing IWC of the cloud: sublimation forms a strong cooling anomaly, associated with a downdraft at and just below the wavy cloud base (Figure 3e). A deposition-driven heating anomaly in the center of the cloud sustains an updraft motion, which in turn leads to more vapor deposition (Figure 3e). However, the cloud top is still dominated by radiative cooling (Figure S1), driving a downdraft motion which helps sustain a small mixed layer at the boundary of the radiative cooling and the latent-heating-driven updraft (Figure 3h).

The diabatic heating not only drives vertical motions within cloud but also supports a circulation pattern as shown by Figures 3j–3l, which reaches its maximum around 4–5 hr after the beginning of the simulation. The circulation develops a two-cell motion:

- a radiatively driven circulation with a strong outflow at about 11–12 km and an equally strong inflow near the cloud top, between 13 and 14 km altitude (Figure 3 k).
- a latent-heating-driven circulation near cloud base, with an outflow below cloud base, and an inflow just above it.

The upper branch of the circulation leads to formation of a tropopause thin cirrus (Figures 3b and 3c). The origin of the cloud can be traced back to the radiatively driven inflow and the associated convergence of air, which cuts off the uppermost cloud layers, and leads to an updraft just above cloud top (Figure 3k). The

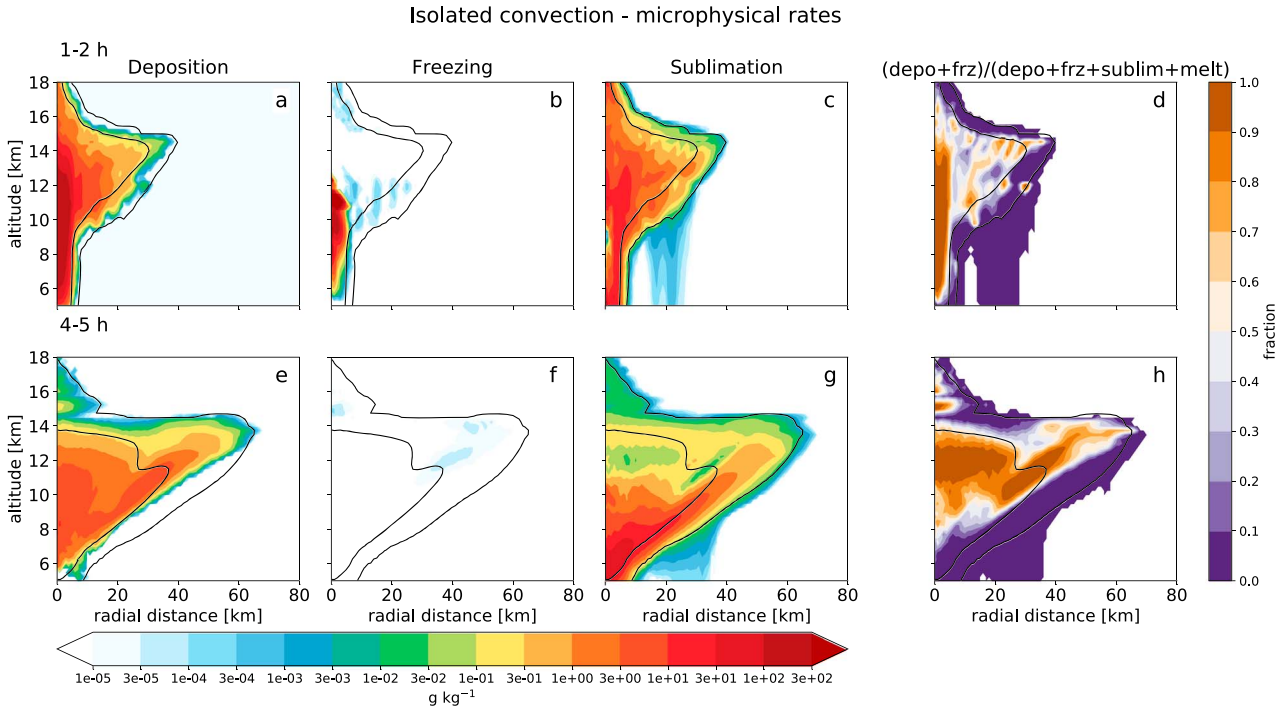

Figure 6. Evolution of the selected microphysical process rates for the isolated convective case (a–c and e–g). The panels (d) and (h) represent the ratio between the absolute values of sources and sinks. The black contour lines represent ice water content contours of 0.1 and 0.0001 g/kg.

updraft is further intensified by depositional heating and new IC nucleation events. The tropopause cirrus is long lived, as it is shielded from the terrestrial LW heating by the underlying anvil cloud, as discussed in Hartmann et al. (2001). The circulation pattern moves together with the cloud edge (Figures 3i and 3l), slowly decaying with the gradual sublimation and sedimentation of the cloud. Interestingly, a vigorous updraft continues to sustain the tropopause cirrus even when the anvil has substantially thinned (Figures 3c and 3i). This later stage is characterized by vertically stratified pancake-like laminar motions with only minimal vertical wind components, similarly to what was found by Dinh et al. (2010) for thin tropopause cirrus.

4.2.3. Impact of the Selected Processes on the CREs

Most of the processes that we examine significantly influence the net CRE of the anvil cloud life cycle. The control simulation yields a small negative net CRE over the course of its life cycle (Figure 2a). The simulation in which the ACRE were turned off (*NO ACRE*) yields a more negative CRE, as the cloud does not spread and thins due to the absence of radiatively driven circulations and in-cloud convective motions (Figure 4b). By limiting the nucleation of new ICs we also limit the formation of thin cirrus, leading to a significantly more negative net CRE (Figure 4f). On the other hand, keeping the ICs aloft by not allowing them to sediment increases the net CRE which becomes significantly positive (Figure 4c). *NO SUBI* and *NO DEPO* simulations both yield a net negative integrated CRE over the course of 14 hr (Figures 4d and 4e). Inhibiting sublimation results in the lack of particle removal and weaker circulations. Inhibiting deposition, on the other hand, drastically increases the production of new, radiatively very active small ICs, which have both a strong LW and SW CRE. Interestingly, the lack of deposition leads to an erosion of the internal parts of the cloud, which are normally dominated by depositional growth of ICs (Figure 4e). The tropopause cirrus cannot form in *NO ACRE* and *NO DEPO* simulations (Figures 4b and 4d) but is still able to form weakly in *NO NUCI* (Figure 4e). The tropopause cirrus therefore consists of both preexisiting anvil cloud ICs and the newly nucleated ICs.

4.3. Isolated Convection

The first deep convective activity develops at the location of the initial moist bubble. The moist air is buoyant and rises, forms clouds, and therefore gains more energy for its ascent due to the latent heating of condensation. About 1 hr from the beginning of the simulation, the convective cloud crosses the homogeneous freezing temperature for water, forming ICs and releasing more latent heat to the environment, which pushes the updraft up to 18 km altitude (Figures 5a, 5b, 6a, 6d, and 6g). Despite developing a significant

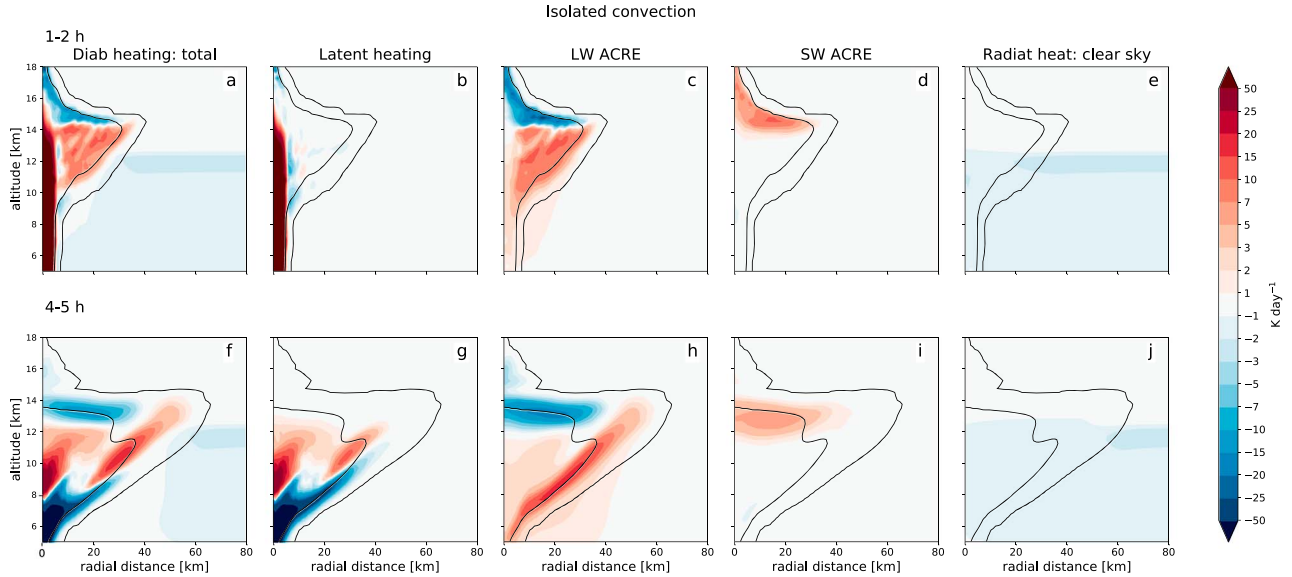

Figure 7. Decomposition of the diabatic heating sources for isolated convection (a–j). Black contour lines represent ice water content contours of 0.1 and 0.0001 g/kg. SW = shortwave; LW = longwave; ACRE = atmospheric cloud radiative effects.

radiative heating of up to 20 K/day dominated by its LW component (Figures 7c and 7d), it is the latent heating that dominates the initial cloud development. When the cloud reaches its maximum altitude, it starts to spread horizontally at velocities of 5–8 m/s (Figure 9). The convectively driven latent heating also dictates the circulation pattern with a large updraft fed by the surface inflow, and detraining ICs between 12- and 15-km elevation (Figures 7b, 8a, and 8b). The large initial heating is a vigorous source of gravity waves (Bretherton, 1988; Prasad et al., 2019), which significantly perturb the instantaneous wind fields while not influencing the mean winds.

The first phase ends after ~3 hr, when the cloud spreading velocity temporarily slows down, before increasing again to about 2 m/s (Figure 9). At this stage, when the cloud still contains a large IWC yielding an optical depth of 11 (Figure 5b), the radiative driving becomes the dominant factor for the development of the cloud (Figures 7h, 7i, and 8h). The spreading velocity of the *NO ACRE* experiment reaches values close to zero between 3 and 4 hr from the start of the simulation (Figure 9). The cloud stops spreading and remains in the relatively thick anvil stage for longer compared with the control simulation.

At hours 4–5 of the simulation, a diabatic heating "sandwich" pattern forms (Figure 5e), including the following:

- LW radiative cooling of about 15 K/day at the cloud top, partially canceled by SW radiative heating of about 5 K/day (Figures 7h and 7i);
- LW radiative heating at the cloud base with values between 2 and 15 K/day (Figure 7h);
- Latent heating by deposition contributes to most of the heating (3–30 K/day) between 8- and 12-km altitude in the core of the cloud (Figure 7g, 6e, and 6h);
- Latent cooling by sublimation dominates the base of the cloud, reaching values of more than −50 K/day (Figure 7g).

A reflection of the heating "sandwich" is seen in vertical velocity: a downdraft of up to 0.5 m/s at the cloud base, updrafts in the center and at the edges of the cloud of 0.05 to 0.2 m/s and a downwelling motion near cloud top (Figure 5h). There are no clear boundaries between the updrafts and downdrafts, as two mixed layers form: one just below the cloud top and one in the central part of the cloud. Interestingly, deposition and sublimation often occur in what looks like the same location due to azimuthal and time averaging (Figures 6e and 6g). The cooccurrence of deposition in sublimation is further supported by the highly turbulent cloud interior with several small convective cells, which gives rise to an uneven cloud top and cloud base, reminiscent of mammatus clouds (Ferlay et al., 2014; Garrett et al., 2010).

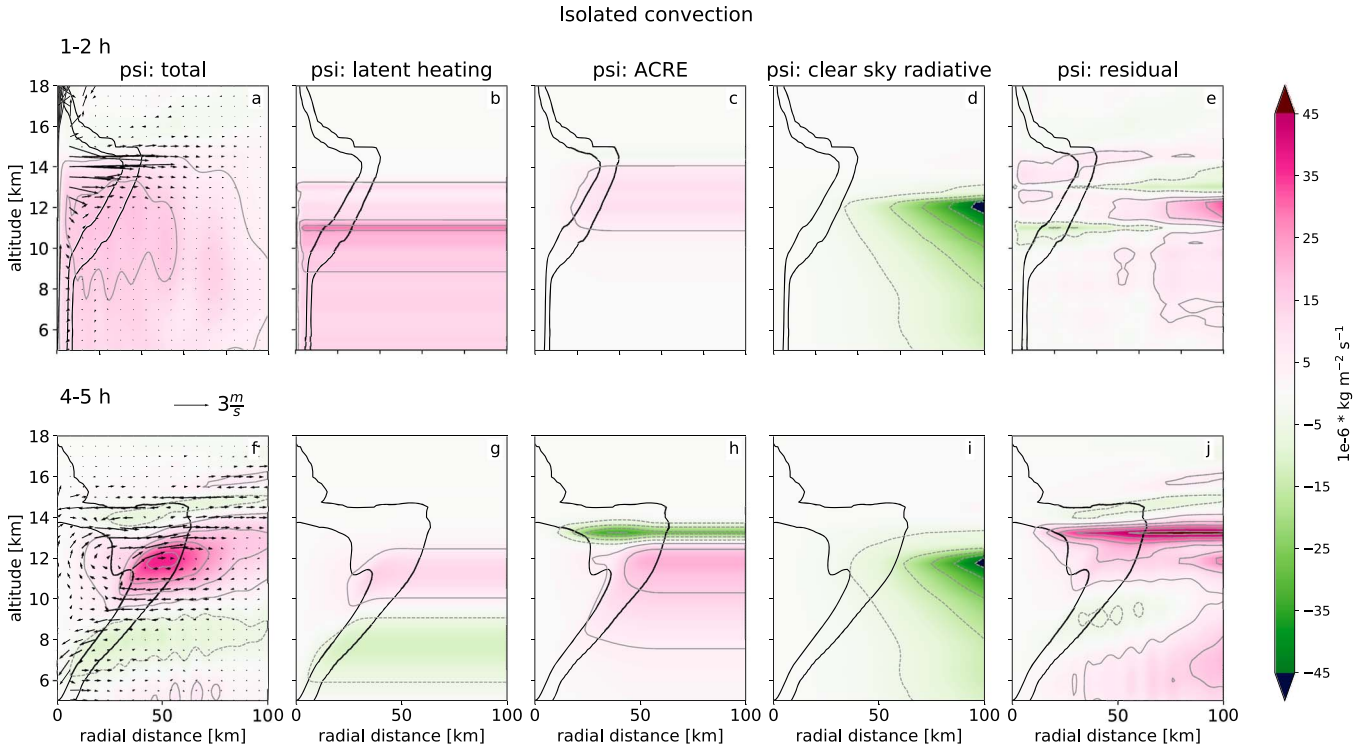

Figure 8. Decomposition of the stream function for isolated convection (a–j). Black contour lines represent ice water content contours of 0.1 and 0.0001 g/kg. The panels a and f show also wind vectors. Vertical winds are multiplied by a factor of 4. ACRE = atmospheric cloud radiative effects.

A strong upper level circulation pattern forms, driven mainly by ACRE and the associated turbulence (Figures 5k, 8f-j), similar to the isolated cloud case. Latent heating is responsible for a weaker circulation close to the cloud base, at elevations between 5 and 10 km. The radiatively-driven inflow at the cloud top forms a thin tropopause cirrus cloud above the anvil cloud (Figure 5b,c).

The final stage of cloud thinning is characterized by a weakening circulation that spreads with the cloud edge (Figure 5c,f,i,l). The thin anvil cloud only slowly sediments due to the effects of radiative heating, which favor updraft motion. The radiative heating is strongest near the spreading front, and weaker in the middle of the cloud, which sinks to lower levels, forming a bowl-shaped cloud top with the tropopause cloud above (Figure 5f,i). The magnitude of microphysical rates decrease, with sublimation becoming dominant over the deposition and freezing (Figure 6e-h). The clear-sky radiation drives part of the circulation only at the domain edges, where there is no stronger source of diabatic heating (Figures 7e,j and 8d,i).

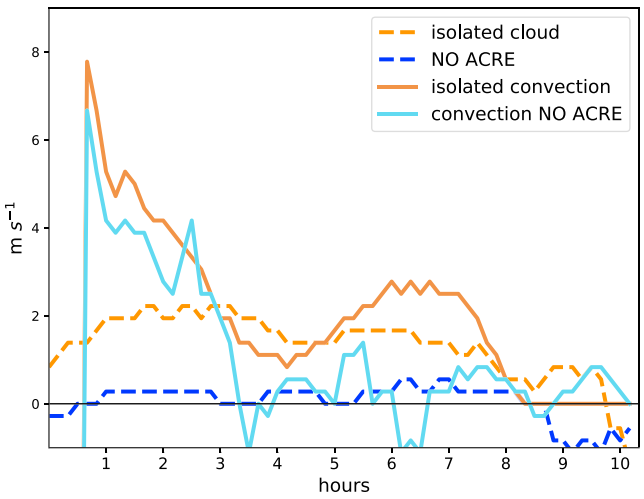

Figure 9. Spreading velocity of the cloud for isolated cloud and isolated convective simulations. The velocity is calculated from the azimuthally averaged IWP spreading front defined by the outermost grid point that reaches IWP value of 0.005 g/m^2. IWP = ice water path; ACRE = atmospheric cloud radiative effects.

4.4. RCE

Finally, we analyze the contribution of several processes to the diabatic heating and circulation in a 80-day long simulation in radiative convective equilibrium with no daily cycle of insolation. We analyze 48 timesteps (one every 2 hours) of output data from days 70-74 of the simulation. We bin all gridpoints by their respective IWP in 50 bins, rather than attempt to detect and evaluate numerous convective life cycles. The total diabatic heating reveals a familiar “sandwich” pattern with a strong in-cloud warming in the most ice-filled bins with cooling anomalies above (radiative cloud top cooling) and below it (sublimation), and a slightly negative background heating rate due to the LW emission by water vapor (Figure 10d). We apply the method from Bretherton et al. (2005) to derive the mass stream function by integrating the vertical

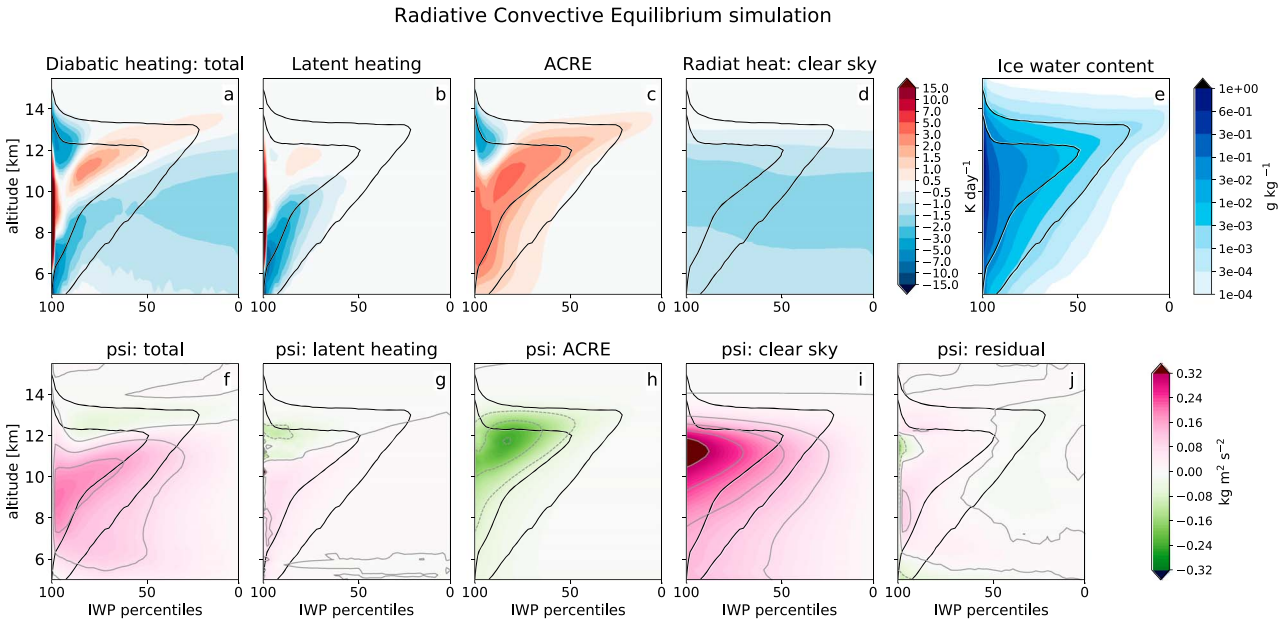

Figure 10. Decomposition of diabatic heating and stream function into its components for the radiative convective equilibrium simulation (a–d and f–j). Panel (e) shows ice water content. Black contour lines represent cloud fractions of 0.1 and 0.5. IWP = ice water path; ACRE = atmospheric cloud radiative effects.

velocities in IWP binned columns. These results sample numerous convective systems with different properties and cloud top/base levels. Therefore we do not expect as sharp and strong circulation patterns as in our idealized simulations. Nevertheless, the reconstruction gives a circulation pattern with an inflow at levels below 10 km, outflow at 11-13 km, and an inflow just above the cloud top at 13-14 km (Figure 10f), which is consistent with the idealized experiments. The stream function decomposition reveals important contributions to the circulation from both cloudy and clear-sky radiative effects, with a minor latent heating component (Figure 10g-j). Unlike in the idealized experiments, the clear-sky component drives a large fraction of the circulation (Figure 10i). The IWP binning gives equilibrium/climatological values; a high IWP is therefore well correlated with high moisture content, explaining the large clear-sky component of the stream function. The clear-sky cooling does not play a large role in idealized experiments, as the water vapor does not have enough time to fully adapt to the convective perturbation. The inclusion of the diurnal cycle modulates the convective activity: the precipitation peaks in the early morning hours before the sunrise, while the anvil cloud cover and IWP peak between 9-11 a.m. local time. However, the controls of the anvil life cycle do not change when averaged over the course of several diurnal cycles, representative of climatological mean values (Figure S6).

4.5. Model Resolution Dependence

The horizontal grid spacing of 1 km only resolves part of the turbulent motions generated by the strong radiative and latent heating; the rest is generated by the subgrid turbulence scheme. To test the sensitivity of the results to the horizontal resolution we perform simulations of varying resolutions in the RCE setup. Increased model resolution increases the ratio of thin versus all cirrus clouds, leading to a more positive net CRE (Figure 11a). The main mechanisms leading to this resolution dependence are likely the turbulent motions, which are mainly parameterized at low resolutions and resolved at high resolutions. This is in contrast to Khairoutdinov et al. (2009), who found similar high cloud cover for horizontal resolutions of up to 1,600 m compared with the 100-m benchmark simulation. However, they nudged the domain-averaged thermodynamic fields and winds to the GATE Phase III field experiment observations (Fu et al., 1995) and used a simpler, one-moment microphysical scheme.

To better understand the effects of increased vertical and horizontal resolution on a single cloud life cycle, we perform two additional simulations in the isolated convection setup:

- *VRES_con* in which we increase only the vertical resolution to 50 m between 8 and 15 km (while the layers between 5.5 and 8 km and 15 to 16.5 km have a resolution between 50 and 100 m);

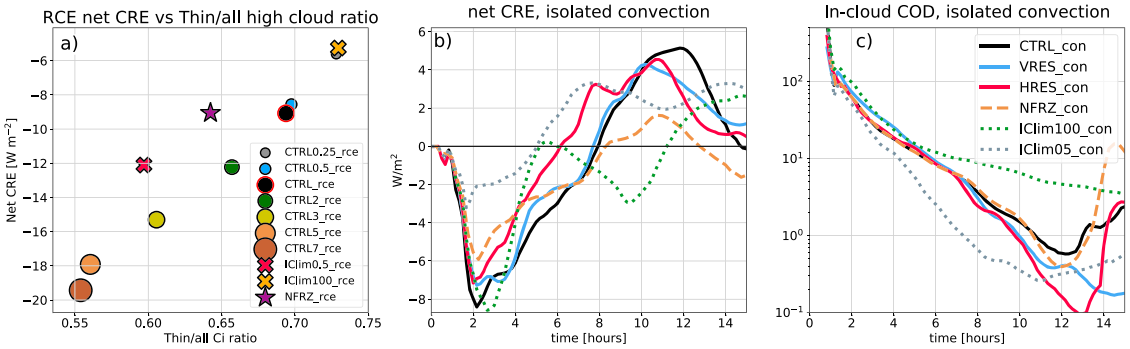

Figure 11. Sensitivity simulations for radiative convective equilibrium (RCE, a) and isolated convection (b, c) setups. (a) The ratio of thin versus all cirrus where thin cirrus are all high clouds that have a net positive CRE, that is, with COD larger than 4. (b, c) Time evolution of domain-averaged net CRE and in-cloud COD for the isolated convective simulations. In (b) only the middle 160 km of the domain are considered, to account for the smaller horizontal grid dimension in *HRES_con*. CRE = cloud radiative effects; COD = cloud optical depth.

- *HRES_con* in which we increase the horizontal resolution to 250 m and use the high vertical resolution from *VRES_con*.

The effects of increased vertical resolution to anvil properties and radiative effects are small (Figures 11b and 11c): the removal of IWC from the thicker part of the anvil is faster, which decreases the LW and SW CRE, accelerates the anvil evolution, and decreases its spreading. When additionally increasing the horizontal resolution, the cloud follows a similar evolution pattern in terms of averaged COD and its domain-averaged radiative effects (Figures 11b and 11c). The cloud covers a smaller area, which might be an artifact of a smaller horizontal model domain (160 km compared to 256 km). Interestingly, a closer look at the temporal evolution reveals significantly larger SW and LW CRE compared to *CTRL_con* and *VRES_con*. The finer horizontal resolution more than compensates for the faster IWC removal in the *VRES_con* simulation, leading to a thicker, more net CRE negative core of the cloud, and generating more clouds in the COD range of 0.3 to 3, which yield a larger LW CRE (Figure S7). In summary, while increased horizontal and/or vertical resolution has an influence on the microphysical process rates and removal of ice from the atmosphere, it does not significantly change the evolution pathway nor the conclusions of our work.

4.6. Microphysical Sensitivity Tests

As the simulations of anvil cloud evolution were found to be very sensitive to details in the description of microphysics (Ohno & Satoh, 2018; Powell et al., 2012), we perform several microphysical sensitivity tests. In particular, we vary the upper limit of IC number concentration and implement a more realistic freezing scheme for temperatures below the homogeneous freezing temperature of water.

We perform simulations in which we change the upper IC number limit used in our simulations (10×10^6 kg^{-1}) to

- 0.5×10^6 kg^{-1} as used in the default P3 scheme;
- 100×10^6 kg^{-1}.

The fraction of thin cirrus increases proportionally with the upper limit of ICs. Consequently, IClim0.5_rce decreases the net CRE by about 3 W/m^2, compared to the CTRL_rce simulation, while the IClim100_rce has just the opposite effect (Figure 11a). Interestingly, the impact on the single convective cloud and its life cycle is different: decreasing the limit does not allow the initial formation of a very thick anvil cloud, and leads to a thinner and smaller cloud, with a more positive net CRE. On the other hand, IClim100_conv allows a formation of a thicker and longer-lived cloud, which, however, does not change its integrated CRE much over the course of the convective life cycle (Figures 11b and 11c).

Despite large disagreements about the radiative and microphysical importance of small ICs and the possibility of new nucleating events in the later stages of anvil evolution (Jensen et al., 2009; Protat et al., 2011; Whiteway et al., 2004), we perform an additional sensitivity test by changing the freezing parameterization below the homogeneous freezing temperature of water (−38 °C). In P3 the deposition freezing parameterization by Cooper (1986), valid in the mixed-phase temperature range, is used also at temperatures colder than −38 °C, leading to an overestimation of freezing events. The high number of newly nucleated ICs at cirrus

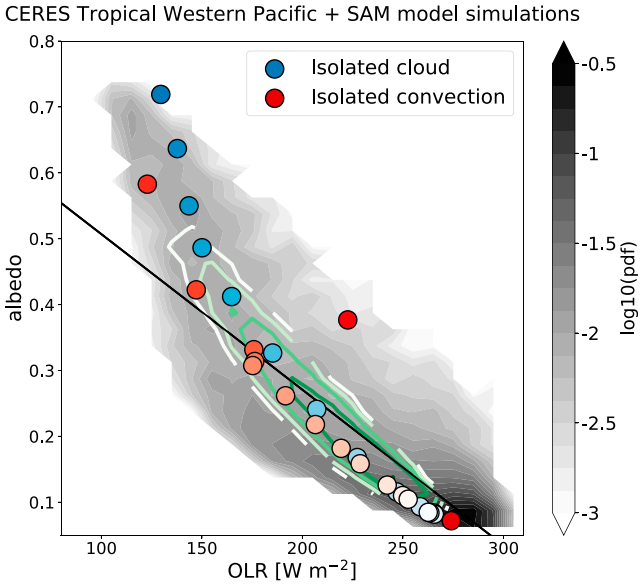

Figure 12. Probability density of outgoing longwave and albedo from CERES pixel measurements from the tropical western Pacific (12°S to 12°N, 150°E to 170°E). The green contour lines show the same distribution derived from the radiative convective equilibrium simulation. Blue circles represent the average over the cloudy part of the domain for the isolated cloud case, while the red circles represent the same for the isolated convective case. The circles are spaced by 1 simulation hour; the color of the circles is fading together with the time evolution of the cloud. The black line indicates the approximate location of the net cloud radiative effects (CRE) neutral line. Points above the line have a negative net CRE, while those below it a positive net CRE.

levels is therefore limited by the upper IC number limit. We try to avoid the frequent use of the unphysical IC limit by parameterizing the freezing at temperatures colder than −38 °C using the homogeneous freezing scheme from Liu and Penner (2005), and a heterogeneous freezing based on the laboratory results from Möhler et al. (2006). The heterogeneous freezing scheme assumes a dust concentration of 2 ice nucleating particles per liter. This number is based on the simulated dust concentrations in TWP by ECHAM-HAM climate model (Gasparini & Lohmann, 2016). Interestingly, the implementation of the new freezing scheme (*NFRZ_rce*) does not change the net CRE, despite forming about 5% less thin cirrus compared to *CTRL_rce* (Fig 11a). *NFRZ_conv* decreases the lifetime of the detrained anvil cloud due to a decrease in the frequency of ice nucleation events, but does not change the net CRE integrated over the whole anvil life cycle (Figures 11b and 11c). Such behavior may also explain why the net CRE balance does not change between the control and *NFRZ_rce* simulations.

4.7. Modeling Results in the Context of the Observed Cloud Radiative Properties

Figure 12 shows the observed probability density function of the outgoing LW radiation (OLR)—albedo pairings for the TWP during July and August as described in Hartmann and Berry (2017). The green contours represent the analogous PDF computed from the 80-day long RCE simulation, averaged to 32 × 32 km to correspond with the observed CERES pixel dimensions. They follow the peak of the observed distribution but show less variability in both albedo and OLR. The smaller number of sample points resulting from horizontal averaging, together with the absence of large-scale dynamical variability are responsible for its smaller spread compared with observations. Moreover, the mode of the distribution is shifted toward larger albedo and smaller OLR values, indicative of an overestimation of thin cirrus. On the other hand, the isolated cloud simulation follows the peak of the observed PDF but starts at a higher OLR indicative of a too low cloud top compared to the observed deep convective clouds. The isolated convection simulation differs from the isolated cloud simulation in that it starts at clear-sky conditions, quickly grows to a high albedo and low OLR deep convective core, which gradually thins by following the peak of the observed PDF. After about 14 hr, the first convective life cycle reaches the final thin cirrus stage, with the radiative properties very close to the initial clear-sky conditions. Moreover, the duration of the convective life cycle qualitatively agrees with the results from Wall et al. (2018), which were able to track the tropical convective systems with geostationary satellite data for about 10 hr after the peak of convective activity. Figure 12 shows that our idealized modeling setup can reproduce average aspects of the tropical cloud radiative properties and its evolution, supporting our main findings of the importance of diabatic processes on the anvil cloud evolution.

5. Discussion

5.1. Drivers of Anvil Evolution

Our results largely agree with previous literature on the importance of ACRE for the maintenance and radiative effects of the anvil life cycle. Simulations without the effects of ACRE could not achieve a near cancelation of the SW and LW CRE as observed in the deep tropics, leading instead to a strongly negative net CRE. Radiative heating promotes the formation and maintentance of thin anvils, which is similar to the results by Hartmann et al. (2018) who used a very simple cloud geometry. We find the horizontal spreading of the cloud to be the key feature influencing the radiative effects integrated over the whole convective life cycle. We attributed a large share of the spreading to the in-atmospheric cloud radiative heating, as the cloud did not spread in the *NO ACRE* simulation. On the other hand, in the climatologically relevant RCE simulation, the cloud processes change the distribution of water vapor, which in turn drives a large part of the upper tropospheric cloud-scale circulation.

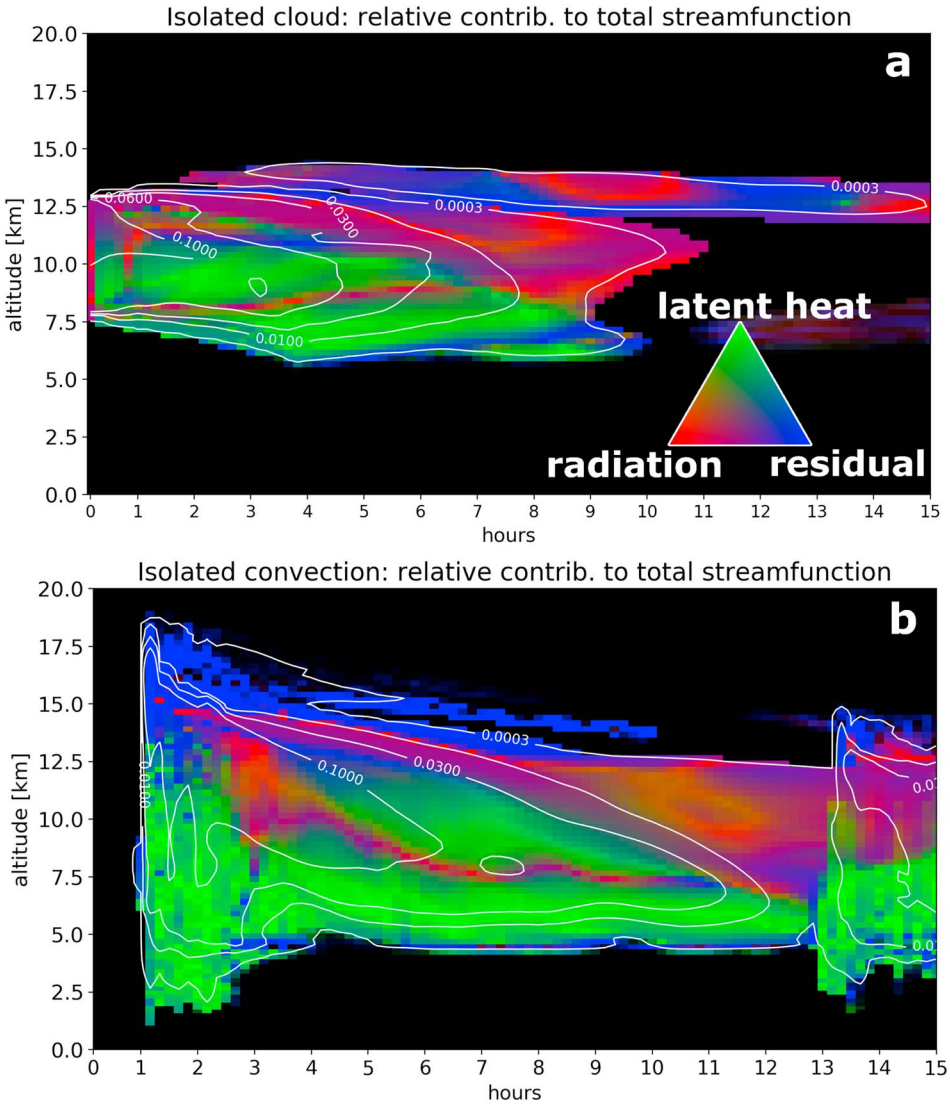

Figure 13. Relative importance of radiation (red), latent heating (green), and the residual (blue, mainly related to turbulent motions) to the total stream function for the isolated cloud (a) and isolated convection (b). White contours represent equal ice water content lines, with the values corresponding to domain averages. The stream function contributions are averaged over all areas in the domain, where ice water content is present. A mixture of colors represents a mixture of processes.

Our main conclusions differ from a modeling study by Jensen et al. (2018), in which they followed trajectories of ICs detrained from a midlatitude thunderstorm and simulated the first 3 hr of their microphysical evolution. Their results show the importance of gravitational settling and depositional growth. However, due to the lack of radiative coupling, they could not observe any convective overturning within the anvil cloud. Interestingly, in the simulations described in sections 4.2 and 4.3, a thin and long-lived tropopause cirrus formed above the anvil, a thin and long-lived tropopause cirrus formed in both idealized modeling setups. This is similar to aircraft observations of Garrett et al. (2005) who observed a similar formation of a long-lived overshooting thin cirrus.

The isolated cloud case closely follows the thick cirrus simulation from Schmidt and Garrett (2013). While they studied only the first hour of a high-resolution limited-area model output, we used a coarser resolution and a larger domain size to be able to monitor later stages of cloud evolution. Similarly to their study, we find the early stage of evolution in the isolated cloud setup to be dominated by radiatively driven turbulence at the cloud top and cloud base and the spreading mixed layer (Figure 13a). After a few minutes of simulations, however, the contribution from latent heating and cooling become dominant in the lower half of the

cloud, while the upper third of the cloud is dominated by the radiatively driven circulations throughout the life cycle. The contribution of latent heating gradually decreases with the thinning of the cloud, when the turbulence is replaced by weaker motions, mainly radiatively driven.

The isolated cloud simulations qualitatively agree with the Lilly (1988) model of the deep convective outflow as an intrusion of nearly equally buoyant air with isotropic turbulence into stably stratified environmental air. The initial convective outflow can be thought of as a large spherical air parcel. When the parcel hits the stable environment with potential temperature increasing with height, it has to flatten to form a pancake-like spreading pattern and generate predominantly horizontal and isentropic laminar flows (Figures 3j–3l).

The later stage of the isolated convective case evolution is, similar to the isolated cloud case, dominated by a combination of radiative and turbulent driving at the cloud top and latent heating at the cloud base, which gradually decreases in strength due to the thinning of the cloud and the smaller microphysical process rates (Figure 13b). At hour 13 of the simulation, new convective activity starts, which again increases the significance of latent heating. Our study highlights the importance of the interaction of radiative and latent processes for the in-cloud convection and inhomogeneities, agreeing with results from Dobbie and Jonas (2001) that studied cirrus of COD between 1 and 2.

We have shown how an isolated deep convective system in the absence of large-scale ascent evolves until it reaches the thin cirrus stage. At this stage, the cloud properties are similar to those observed in persistent tropical tropopause cirrus, which have been found to be in a delicate balance between microphysics, radiation, and the generated internal cloud dynamics (Dinh et al., 2010, 2012). The evolution of both our idealized cloud and isolated convection suggest that the anvil cloud ends its life cycle by a transition to a similar self-sustained thin cirrus stage.

5.2. Shortcomings of the Modeling Setup

The absence of ocean coupling and the relatively small domain prevents us from studying other proposed mechanisms behind the triggering and occurrence of tropical deep convection and its CRE budget. Ramanathan and Collins (1991) and Hartmann et al. (2001) proposed a mechanism that couples tropical convection, the associated cloud albedo, sea surface temperatures, and atmospheric circulations by a self-regulating feedback process. Wall et al.'s (2018) observational study also supports the idea of a tight coupling between the triggering of deep convection and the sea surface temperatures in the TWP. Our idealized study rather focuses on the drivers of the evolution of convection and the detrained anvil clouds, once the conditions are right for its triggering. Our primary focus is on the subdaily scale, which is too short to be significantly affecting sea surface temperatures. Sea surface temperature mediated feedbacks have been found to influence simulations in an RCE setup (Coppin & Bony, 2017) and will therefore be included in our future work.

Convective strength, anvil cloud extent, and their properties are also modulated by the daily cycle of insolation (Chen & Houze, 1997; Dai, 2001). Ruppert and Klocke (2019) show that the diurnal peak in the cloud radiative heating increases the vertical velocities within anvils and leads to an anvil cloud peak in the afternoon. Similarly, the anvil life cycle was found to be suppressed during nighttime. The inclusion of the daily cycle of insolation was found to modulate the cloud evolution and radiative effects, although not in the climatological sense (Figure S6). In addition, the cloud evolution in our study is simulated in the absence of a large-scale forcing and also cannot feed back on larger-scale circulations. Therefore, the gravity waves generated by the initial burst of convection can return back toward the middle of the domain via the periodic horizontal boundary conditions. Figure 12 shows, however, that the listed shortcomings do not prevent us from simulating clouds that fit within the range of the observations from the TWP.

6. Conclusions

The net CRE in the tropics range from very negative, SW-dominated deep convective cores, to near-neutral or moderately positive for intermediately thick anvil clouds, to positive for thin anvils and other high clouds that are not directly related to detrained ice from convection. The convective life cycle starts with a convective instability and updraft motion. Updrafts are associated with a large latent heat release due to cloud droplet condensation and freezing, and depositional growth of newly nucleated ice crystals. Latent heat release is the dominant factor in the deep circulation pattern that develops in the early convective stage, with the low level inflow, upper level outflow, and the slow subsidence far from the convective core. This circulation is

also responsible for the large initial spreading of the cloud, reaching horizontal velocities beyond 5 m/s. About 3 hr after the convective initiation, the cloud has spread horizontally more than 50 km from the convective core, developing a thick stratiform anvil with a strong sandwich-like heating pattern, which can be summarized by

- a LW cooling at the cloud top;
- a LW warming at and near the cloud base and cloud edge;
- additional warming in the cloud interior by latent heating due to the depositional growth of ice crystals; and
- a strong cooling at and just below the cloud base due to ice crystal sublimation.

The differential heating and cooling are found to drive within-anvil turbulent motions at horizontal scales smaller than 5–10 km. However, the mixed layer does not spread through the whole cloud: in fact, we observe a strong small-scale overturning below the cloud top, and a weaker one close to the cloud base. While the radiative and latent contributions are closely related, we find the upper third of the cloud to be predominantly driven by ACREs. In contrast, latent heating drives the evolution and circulations in the lower part of the cloud. Within-anvil convection and turbulence slowly decrease in strength with the thinning and spreading of the cloud, until the laminar motions become dominant at cloud optical depths between about 5 and 10. Interestingly, the radiatively driven circulation at the cloud top is responsible for the formation of thin tropopause cirrus. The results of the idealized isolated cloud and isolated convective simulations qualitatively agree with averages from the radiatively convective equilibrium simulation, with the exception of the clear-sky effects which are very important in RCE (Hartmann & Larson, 2002).

Our findings confirm that small-scale processes are important for the anvil cloud life cycle. Such microphysical, radiative, and dynamical processes significantly impact the cloud development and hence CRE and climate. Current general circulation models, which are used for future climate and cloud feedback estimates, have upper tropospheric vertical and horizontal resolutions orders of magnitude larger than the scales discussed in this work and often have difficulties in simulating anvil clouds (Wall & Hartmann, 2018). Results from studies on high cloud responses to increased greenhouse gas concentrations (Bony et al., 2016; Hartmann & Larson, 2002; Mauritsen & Stevens, 2015) using crude descriptions of the small-scale processes should therefore be revisited. The new generation of global climate models, even those able to directly simulate deep convection, might still not simulate the small-scale processes driving the anvil evolution in a reliable way. Our idealized modeling setup could therefore provide a benchmark for parameterizations in models both with parameterized and resolved deep convection.

Acknowledgments
We acknowledge support from the Swiss National Science Foundation Grant P2EZP2-178485 (B. G.), National Science Foundation through Grant ATG-1549579 (B. G. and P. B.), Department of Energy (DOE) Office of Science Early Career Award Program (J. F.). The work of coupling P3 with SAM was carried out by G. L. and J. F. who were supported by the Climate Model Development and Validation program of the DOE Climate and Environmental Sciences Division. We acknowledge Phil Rasch and Marina Dütsch for insightful discussions that improved this study. We acknowledge Tra Dinh and one anonymous reviewer for constructive comments. Data and analysis scripts necessary to generate the figures are available at 10.5281/zenodo.3333030. The satellite data from the A-Train Integrated CALIPSO, CloudSat, CERES, and MODIS Merged Product Release B1 (CCCM) were obtained from https://search.earthdata.nasa.gov.

References

Ackerman, T. P., Liou, K.-N., Valero, P. J. F., & Pfister, L. (1988). Heating rates in tropical anvils. *Journal of Atmospheric Sciences*, *45*(10), 1606–1623.

Berry, E., & Mace, G. G. (2014). Cloud properties and radiative effects of the Asian summer monsoon derived from A-Train data. *Journal of Geophysical Research: Atmospheres*, *119*, 9492–9508. https://doi.org/10.1002/2014JD021458

Bony, S., Stevens, B., Coppin, D., Becker, T., Reed, K. A., Voigt, A., & Medeiros, B. (2016). Thermodynamic control of anvil cloud amount. *Proceedings of the National Academy of Sciences*, *113*(32), 8927–8932. https://doi.org/10.1073/pnas.1601472113

Bretherton, C. (1988). Group velocity and the linear response of stratified fluids to internal heat or mass sources. *Journal of the Atmospheric Sciences*, *45*(1), 81–94. https://doi.org/10.1175/1520-0469(1988)045h0081:gvatlri2.0.co;2

Bretherton, C. S., Blossey, P. N., & Khairoutdinov, M. (2005). An energy-balance analysis of deep convective self-aggregation above uniform SST. *Journal of Atmospheric Sciences*, *62*, 4273–4292. https://doi.org/10.1175/jas3614.1

Charney, J. G. (1963). A note on large-scale motions of the tropics. *Journal of the Atmospheric Sciences*, *20*, 607–609.

Chen, S. S., & Houze, R. A. Jr. (1997). Diurnal variation and life-cycle of deep convective systems over the tropical Pacific warm pool. *Quarterly Journal of the Royal Meteorological Society*, *123*(538), 357–388.

Cooper, W. A. (1986). Ice initiation in natural clouds. *Meteorological Monographs*, *43*, 29–32. https://doi.org/10.1175/0065-9401-21.43.29

Coppin, D., & Bony, S. (2017). Internal variability in a coupled general circulation model in radiative-convective equilibrium. *Geophysical Research Letters*, *44*, 5142–5149. https://doi.org/10.1002/2017GL073658

Dai, A. (2001). Global precipitation and thunderstorm frequencies. Part II: Diurnal variations. *Journal of Climate*, *14*(6), 1112–1128. https://doi.org/10.1175/1520-0442(2001)014h1112:GPATFPi2.0.CO;2

Dinh, T. P., Durran, D. R., & Ackerman, T. P. (2010). Maintenance of tropical tropopause layer cirrus. *Journal of Geophysical Research*, *115*, D02104. https://doi.org/10.1029/2009JD012735

Dinh, T., Durran, D. R., & Ackerman, T. (2012). Cirrus and water vapor transport in the tropical tropopause layer Part 1: A specific case modeling study. *Atmospheric Chemistry and Physics*, *12*(20), 9799–9815. https://doi.org/10.5194/acp-12-9799-2012

Dobbie, S., & Jonas, P. (2001). Radiative influences on the structure and lifetime of cirrus clouds. *Quarterly Journal of the Royal Meteorological Society*, *127*(578), 2663–2682.

Durran, D. R., Dinh, T., Ammerman, M., & Ackerman, T. (2009). The mesoscale dynamics of thin tropical tropopause cirrus. *Journal of the Atmospheric Sciences*, *66*(9), 2859–2873. https://doi.org/10.1175/2009jas3046.1

Fan, J., Comstock, J. M., & Ovchinnikov, M. (2010). The cloud condensation nuclei and ice nuclei effects on tropical anvil characteristics and water vapor of the tropical tropopause layer. *Environmental Research Letters*, *5*(4), 044005. https://doi.org/10.1088/1748-9326/5/4/044005

Fan, J., Leung, L. R., Rosenfeld, D., Chen, Q., Li, Z., Zhang, J., & Yan, H. (2013). Microphysical effects determine macrophysical response for aerosol impacts on deep convective clouds. *Proceedings of the National Academy of Sciences*, *110*(48), E4581–E4590. https://doi.org/10.1073/pnas.1316830110

Ferlay, N., Garrett, T. J., & Minvielle, F. (2014). Satellite observations of an unusual cloud formation near the tropopause. *Journal of the Atmospheric Sciences*, *71*(10), 3801–3815. https://doi.org/10.1175/jas-d-13-0361.1

Fu, Q., Krueger, S. K., & Liou, K. N. (1995). Interactions of radiation and convection in simulated tropical cloud clusters. *Journal of the Atmospheric Sciences*, *52*(9), 1310–1328. https://doi.org/10.1175/1520-0469(1995)052h1310:ioracii2.0.co;2

Garrett, T. J., Navarro, B. C., Twohy, C. H., Jensen, E. J., Baumgardner, D. G., Bui, P. T., et al. (2005). Evolution of a Florida cirrus anvil. *Journal of the Atmospheric Sciences*, *62*(7), 2352–2372. https://doi.org/10.1175/JAS3495.1

Garrett, T. J., Schmidt, C. T., Kihlgren, S., & Cornet, C. (2010). Mammatus clouds as a response to cloud-base radiative heating. *Journal of the Atmospheric Sciences*, *67*(12), 3891–3903. https://doi.org/10.1175/2010JAS3513.1

Gasparini, B., Hartmann, D., Rasch, P., & Qian, Y. (2018). What controls the cloud radiative effects in the tropics or why does it matter if an anvil is thin or thick? presented at 2018 AMS conference, https://ams.confex.com/ams/15CLOUD15ATRAD/webprogram/Paper345703.html

Gasparini, B., & Lohmann, U. (2016). Why cirrus cloud seeding cannot substantially cool the planet. *Journal of Geophysical Research: Atmospheres*, *121*, 4877–4893. https://doi.org/10.1002/2015JD024666

Gasparini, B., Meyer, A., Neubauer, D., Münch, S., & Lohmann, U. (2018). Cirrus cloud properties as seen by the CALIPSO satellite and ECHAM-HAM global climate model. *Journal of Climate*, *31*(5), 1983–2003. https://doi.org/10.1175/JCLI-D-16-0608.1

Gehlot, S., & Quaas, J. (2012). Convection-climate feedbacks in the ECHAM5 general circulation model: Evaluation of cirrus cloud life cycles with ISCCP satellite data from a Lagrangian trajectory perspective. *Journal of Climate*, *25*(15), 5241–5259. https://doi.org/10.1175/JCLI-D-11-00345.1

Harrop, B. E., & Hartmann, D. L. (2016). The role of cloud radiative heating within the atmosphere on the high cloud amount and top-of-atmosphere cloud radiative effect. *Journal of Advances in Modeling Earth Systems*, *6*, 223–248. https://doi.org/10.1002/2013MS000282

Hartmann, D. L., & Berry, S. E. (2017). The balanced radiative effect of tropical anvil clouds. *Journal of Geophysical Research: Atmospheres*, *122*, 5003–5020. https://doi.org/10.1002/2017JD026460

Hartmann, D. L., Gasparini, B., Berry, S. E., & Blossey, P. N. (2018). The life cycle and net radiative effect of tropical anvil clouds. *Journal of Advances in Modeling Earth Systems*, *10*(12), 3012–3029. https://doi.org/10.1029/2018MS001484

Hartmann, D. L., Holton, J. R., & Fu, Q. (2001). The heat balance of the tropical tropopause, cirrus, and stratospheric dehydration. *Geophysical Research Letters*, *28*, 1969–1972.

Hartmann, D. L., & Larson, K. (2002). An important constraint on tropical cloud—Climate feedback. *Geophysical Research Letters*, *29*(20), 1951. https://doi.org/10.1029/2002GL015835

Hartmann, D. L., Moy, L. A., & Fu, Q. (2001). Tropical convection and the energy balance at the top of the atmosphere. *Journal of Climate*, *14*(24), 4495–4511. https://doi.org/10.1175/1520-0442(2001)014h4495:TCATEBi2.0.CO;2

Heymsfield, A. J., Krämer, M., Luebke, A., Brown, P., Cziczo, D. J., Franklin, C., et al. (2017). Cirrus clouds. *Meteorological Monographs*, *58*, 1–2. https://doi.org/10.1175/AMSMONOGRAPHS-D-16-0010.1

Heymsfield, A. J., Krämer, M., Wood, N. B., Gettelman, A., Field, P. R., & Liu, G. (2017). Dependence of the ice water content and snowfall rate on temperature, globally: Comparison of in situ observations, satellite active remote sensing retrievals, and global climate model simulations. *Journal of Applied Meteorology and Climatology*, *56*(1), 189–215. https://doi.org/10.1175/JAMC-D-16-0230.1

Houze, R. A. Jr. (1982). Clusters and large-scale in the tropics vertical motions. *Journal of the Meteorological Society of Japan*, *60*(1), 396–410.

Iacono, M. J., Delamere, J. S., Mlawer, E. J., Shephard, M. W., Clough, S. A., & Collins, W. D. (2008). Radiative forcing by long-lived greenhouse gases: Calculations with the AER radiative transfer models. *Journal of Geophysical Research*, *113*, D13103. https://doi.org/10.1029/2008JD009944

Jackson, R. C., McFarquhar, G. M., Fridlind, A. M., & Atlas, R. (2015). The dependence of cirrus gamma size distributions expressed as volumes in N0-λ-μ phase space and bulk cloud properties on environmental conditions: Results from the Small Ice Particles in Cirrus Experiment (SPARTICUS). *Journal of Geophysical Research : Atmospheres*, *120*, 10,351–10,377. https://doi.org/10.1002/2015JD023492

Jensen, E. J., Pfister, L., Bui, T.-P., Lawson, P., & Baumgardner, D. (2009). Ice nucleation and cloud microphysical properties in tropical tropopause layer cirrus. *Atmospheric Chemistry and Physics Discussions*, *9*, 20,631–20,675. https://doi.org/10.5194/acpd-9-20631-2009

Jensen, E. J., van den Heever, S. C., & Grant, L. D. (2018). The lifecycles of ice crystals detrained from the tops of deep convection. *Journal of Geophysical Research: Atmospheres*, *123*, 9624–9634. https://doi.org/10.1029/2018JD028832

Kato, S., Rose, F. G., Sun-Mack, S., Miller, W. F., Chen, Y., Rutan, D. A., et al. (2011). Improvements of top-of-atmosphere and surface irradiance computations with CALIPSO-, CloudSat-, and MODIS-derived cloud and aerosol properties. *Journal of Geophysical Research*, *116*, D19209. https://doi.org/10.1029/2011JD016050

Khairoutdinov, M. F., Krueger, S. K., Moeng, C.-H., Bogenschutz, P. A., & Randall, D. A. (2009). Large-eddy simulation of maritime deep tropical convection. *Journal of Advances in Modeling Earth Systems*, *1*, 13. https://doi.org/10.3894/james.2009.1.15

Khairoutdinov, M. F., & Randall, D. A. (2003). Cloud resolving modeling of the ARM Summer 1997 IOP : Model formulation , results , uncertainties , and sensitivities. *Journal of the Atmospheric Sciences*, *60*, 607–625. https://doi.org/10.1175/1520-0469(2003)060h0607:CRMOTAi2.0.CO;2

Krämer, M., Rolf, C., Luebke, A., Afchine, A., Spelten, N., Costa, A., et al. (2016). A microphysics guide to cirrus clouds Part 1: Cirrus types. *Atmospheric Chemistry and Physics*, *16*(21), 3463–3483. https://doi.org/10.5194/acpd-15-31537-2015

Lilly, D. K. (1988). Cirrus outflow dynamics. *Journal of the Atmospheric Sciences*, *45*(10), 1594–1605.

Liu, X., & Penner, J. E. (2005). Ice nucleation parameterization for global models. *Meteorologische Zeitschrift*, *14*(4), 499–514. https://doi.org/10.1127/0941-2948/2005/0059

Liu, C., Shige, S., Takayabu, Y. N., & Zipser, E. (2015). Latent heating contribution from precipitation systems with different sizes, depths, and intensities in the tropics. *Journal of Climate*, *28*(1), 186–203. https://doi.org/10.1175/JCLI-D-14-00370.1

Lohmann, U., & Roeckner, E. (1995). Influence of cirrus cloud radiative forcing on climate and climate sensitivity in a general circulation model. *Journal of Geophysical Research*, *100*, 16,305–16,323. https://doi.org/10.1029/95JD01383

Luo, Z., & Rossow, W. B. (2004). Characterizing tropical cirrus life cycle, evolution, and interaction with upper-tropospheric water vapor using Lagrangian trajectory analysis of satellite observations. *Journal of Climate*, *17*, 4541–4563. https://doi.org/10.1175/3222.1

Martins, E., Noel, V., & Chepfer, H. (2011). Properties of cirrus and subvisible cirrus from nighttime Cloud-Aerosol Lidar with Orthogonal Polarization (CALIOP), related to atmospheric dynamics and water vapor. *Journal of Geophysical Research*, *116*, D02208. https://doi.org/10.1029/2010JD014519

Massie, S., Gettelman, A., Randel, W., & Baumgardner, D. (2002). Distribution of tropical cirrus in relation to convection. *Journal of Geophysical Research*, *107*(D21), 4591. https://doi.org/10.1029/2001JD001293

Mauritsen, T., & Stevens, B. (2015). Missing iris effect as a possible cause of muted hydrological change and high climate sensitivity in models. *Nature Geoscience*, *8*(5), 346–351. https://doi.org/10.1038/ngeo2414

Mlawer, E. J., Taubman, J., Brown, P. D., Iacono, M. J., & Clough, S. A. (1997). Radiative transfer for inhomogeneous atmospheres: RRTM, a validated correlated-k model for the longwave. *Journal of Geophysical Research*, *102*, 16,663–16,682. https://doi.org/10.1029/97JD00237

Möhler, O., Field, P. R., Connolly, P., Benz, S., Saathoff, H., Schnaiter, M., et al. (2006). Efficiency of the deposition mode ice nucleation on mineral dust particles. *Atmospheric Chemistry and Physics*, *6*, 3007–3021.

Morrison, H., & Milbrandt, J. A. (2015). Parameterization of Cloud microphysics based on the prediction of bulk ice particle properties. Part I: Scheme description and idealized tests. *Journal of the Atmospheric Sciences*, *72*(1), 287–311. https://doi.org/10.1175/JAS-D-14-0065.1

Ohno, T., & Satoh, M. (2018). Roles of cloud microphysics on cloud responses to sea surface temperatures in radiative-convective equilibrium experiments using a high-resolution global nonhydrostatic model. *Journal of Advances in Modeling Earth Systems*, *10*, 1970–1989. https://doi.org/10.1029/2018ms001386

Ohno, T., Satoh, M., & Noda, A. (2019). Fine vertical resolution radiative convective equilibrium experiments: Roles of turbulent mixing on the high cloud response to sea surface temperatures. *Journal of Advances in Modeling Earth Systems*, *11*, 1–11. https://doi.org/10.1029/2019ms001704

Powell, S. W., Houze, R. A. Jr., Kumar, A., & McFarlane, S. A. (2012). Comparison of simulated and observed continental tropical anvilv clouds and their radiative heating profiles. *Journal of the Atmospheric Sciences*, *69*(9), 2662–2681.

Prasad, A. A., Sherwood, S. C., Reeder, M. J., & Lane, T. P. (2019). Rapidly evolving cirrus clouds modulated by convectively generated gravity waves. *Journal of Geophysical Research: Atmospheres*, *124*, 7327–7338. https://doi.org/10.1029/2019JD030538

Protat, A., Delanoë, J., O'Connor, E. J., & L'Ecuyer, T. S. (2010). The evaluation of CloudSat and CALIPSO ice microphysical products using ground-based cloud radar and lidar observations. *Journal of Atmospheric and Oceanic Technology*, *27*(5), 793–810. https://doi.org/10.1175/2009JTECHA1397.1

Protat, A., McFarquhar, G. M., Um, J., & Delanoë, J. (2011). Obtaining best estimates for the microphysical and radiative properties of tropical ice clouds from TWP-ICE in situ microphysical observations. *Journal of Applied Meteorology and Climatology*, *50*(4), 895–915. https://doi.org/10.1175/2010JAMC2401.1

Protopapadaki, S. E., Stubenrauch, C. J., & Feofilov, A. G. (2017). Upper tropospheric cloud systems derived from IR sounders: Properties of cirrus anvils in the tropics. *Atmospheric Chemistry and Physics*, *17*, 3845–3859. https://doi.org/10.5194/acp-17-3845-2017

Ramanathan, V., Cess, R. D., Harrison, E. F., Minnis, P., Barkstrom, B. R., Ahmad, E., & Hartmann, D. L. (1989). Cloud-radiative forcing and climate: Results from the Earth radiation budget experiment linked references are available on JSTOR for this article: Cloud-Radiative Forcing and Climate : Results from the Eart Radiation Budget Experiment. *Science*, *243*(4887), 57–63.

Ramanathan, V., & Collins, W. (1991). Thermodynamic regulation of ocean warming by cirrus clouds deduced from observations of the 1987 El Ninō. *Nature*, *351*(6321), 27–32. https://doi.org/10.1038/351027a0

Riihimaki, L. D., McFarlane, S. A., Liang, C., Massie, S. T., Beagley, N., & Toth, T. D. (2012). Comparison of methods to determine tropical tropopause layer cirrus formation mechanisms. *Journal of Geophysical Research*, *117*, D06218. https://doi.org/10.1029/2011JD016832

Ruppert, J. H., & Klocke, D. (2019). The two diurnal modes of tropical upward motion. *Geophysical Research Letters*, *46*, 2911–2921. https://doi.org/10.1029/2018GL081806

Sassen, K., Wang, Z., & Liu, D. (2009). Cirrus clouds and deep convection in the tropics: Insights from CALIPSO and CloudSat. *Journal of Geophysical Research*, *114*, D00H06. https://doi.org/10.1029/2009JD011916

Schmidt, C. T., & Garrett, T. J. (2013). A simple framework for the dynamic response of cirrus clouds to local diabatic radiative heating. *Journal of the Atmospheric Sciences*, *70*(5), 1409–1422. https://doi.org/10.1175/JAS-D-12-056.1

Schumacher, C., Houze, R. A. Jr., & Kraucunas, I. (2004). The tropical dynamical response to latent heating estimates derived from the TRMM precipitation radar. *Journal of the Atmospheric Sciences*, *61*(12), 1341–1358. https://doi.org/10.1175/1520-0469(2004)061h1341:TTDRTLi2.0.CO;2

Sobel, A. H., & Bretherton, C. S. (2000). Modeling tropical precipitation in a single column. *Journal of Climate*, *13*(24), 4378–4392. https://doi.org/10.1175/1520-0442(2000)013h4378:MTPIASi2.0.CO;2

Starr, D. O., & Cox, S. K. (1985). Cirrus clouds. Part I: A cirrus cloud model. *Journal of Atmospheric Sciences*, *42*(23), 2663–2681.

Stephens, G. L., Vane, D. G., Tanelli, S., Im, E., Durden, S., Rokey, M., et al. (2008). CloudSat mission: Performance and early science after the first year of operation. *Journal of Geophysical Research*, *114*, D00A18. https://doi.org/10.1029/2008JD009982

Van Diedenhoven, B., Fridlind, A. M., Cairns, B., Ackerman, A. S., & Yorks, J. E. (2016). Vertical variation of ice particle size in convective cloud tops. *Geophysical Research Letters*, *43*, 4586–4593. https://doi.org/10.1002/2016GL068548

Wall, C. J., & Hartmann, D. L. (2018). Balanced cloud radiative effects across a range of dynamical conditions over the tropical West Pacific. *Geophysical Research Letters*, *5*, 490–498. https://doi.org/10.1029/2018GL080046

Wall, C. J., Hartmann, D. L., Thieman, M. M., Smith, W. L., & Minnis, P. (2018). The life cycle of anvil clouds and the top-of-atmosphere radiation balance over the tropical West Pacific. *Journal of Climate*, *31*(24), 10,059–10,080. https://doi.org/10.1175/JCLI-D-18-0154.1

Whiteway, J., Cook, C., Gallagher, M., Choularton, T., Harries, J., Connolly, P., et al. (2004). Anatomy of cirrus clouds: Results from the Emerald airborne campaigns. *Geophysical Research Letters*, *31*, L24102. https://doi.org/10.1029/2004GL021201

Wielicki, B. A., Barkstrom, B. R., Harrison, E. F., Lee, R. B., Smith, G. L., & Cooper, J. E. (1996). Clouds and the Earth's Radiant Energy System (CERES): An Earth observing system experiment. *Bulletin of the American Meteorological Society*, *77*(5), 853–868. https://doi.org/10.1175/1520-0477(1996)077h0853:CATEREi2.0.CO;2

Winker, D. M., Pelon, J., Coakley, J. A., Ackerman, S. A., Charlson, R. J., Colarco, P. R., et al. (2010). The Calipso mission: A global 3D view of aerosols and clouds. *Bulletin of the American Meteorological Society*, *91*(9), 1211–1229. https://doi.org/10.1175/2010BAMS3009.1

Yoneyama, K., Zhang, C., & Long, C. N. (2013). Tracking pulses of the MaddenJulian Oscillation. *Bulletin of the American Meteorological Society*, *94*(12), 1871–1891. https://doi.org/10.1175/bams-d-12-00157.1